organoids

MDPI

Article

High-Throughput Analysis of 3D Cell Culture Oxygen Consumption Using Sensor Arrays: A Novel Platform for Hypoxia/Normoxia Research

Christoph Grün *, Cordula Nies, Magdalena Klesen, Enja Schwarz, Jonah ter Haseborg, Cornelius Dettmer, Christian Beyer, Larissa Funk and Eric Gottwald

Karlsruhe Institute of Technology, Institute of Functional Interfaces, 76131 Karlsruhe, Germany; cordula.nies@kit.edu (C.N.); eric.gottwald@kit.edu (E.G.)
* Correspondence: christoph.gruen@kit.edu; Tel.: +49-721-608-26803

Abstract

Precise control and measurement of the cellular microenvironment, particularly oxygen concentration, are crucial for developing physiologically relevant in vitro models. However, current methods often lack the spatial resolution and throughput needed to investigate complex, oxygen-dependent biological mechanisms in 3D cell cultures. Here, we present an advanced platform based on microcavity arrays featuring integrated, ratiometric oxygen sensors, so-called SensoSpheres. A unique bevel design at the cavity entrance enables the non-invasive, real-time measurement of pericellular oxygen concentration and oxygen gradients. We established protocols for generating spheroids from various cell lines (e.g., HepG2, HeLa) and characterized their metabolic responses under precisely controlled hypoxic, normoxic, and hyperoxic conditions. Using a dose–response assay, we demonstrate the platform's sensitivity in capturing distinct metabolic shifts in response to acetaminophen and cisplatin. Furthermore, we introduce the Oxygen Consumption Recovery Rate (OCRR) as a novel parameter to quantify cellular resilience after exposure to toxic compounds such as cisplatin and acetaminophen. This high-throughput-compatible platform represents a significant methodological advancement, enabling detailed studies of oxygen-dependent cellular processes, drug toxicity, and metabolic adaptation. Its potential for integration into microfluidic systems paves the way for more sophisticated organ-on-chip models, ultimately improving the predictive power of preclinical research.

Keywords: physioxia; hypoxia; oxygen consumption rate; oxygen sensing; dose–response assay; oxygen consumption recovery rate; organoids; oxygen measurement

Academic Editors: Süleyman Ergün and Philipp Wörsdörfer

Received: 3 November 2025
Revised: 7 January 2026
Accepted: 3 February 2026
Published: 6 February 2026

1. Introduction

More than 90% of all drug candidates entering clinical trials fail at this stage [1]. Even when they reach the market, recalls due to safety concerns still occur. A systematic review identified 462 such withdrawals between 1953 and 2013 [2]. While this represents a small fraction of all approved drugs (estimated at 2–3% in North America during that period), the clinical and economic impact is significant, highlighting the limitations of traditional preclinical models. This is largely attributed to insufficient clinical efficacy (40–50%) or toxicity (30%) [1,3,4]. The major reason is inherent to the drug development process itself. Animal experiments still play a crucial role in preclinical research [5], even though the transferability is limited. A striking example is the phase I enzyme cytochrome P450 3A4, which is

central to human metabolism but absent in mice and rats [6]. Consequently, New Approach Methodologies (NAMs) are gaining momentum to bridge this translational gap [7–9]. Among these, 3D cell culture systems are particularly promising. Although it took more than 50 years after the introduction of 3D cell culture [10,11], this culture type has been shown to be preferable for translational relevance, as they better replicate morphology [12], cell–cell and cell–matrix contacts [13], metabolism [14], and differentiation [15].

However, one of the most critical parameters—oxygen—has often been overlooked. Establishing physiological oxygen concentrations (physioxia) in in vitro models is essential [16]. Physioxia refers to the tissue-specific oxygen levels naturally found in living organisms, defining the true cellular normoxia for those cells [17]. Despite being a small molecule, oxygen plays a decisive role in metabolism, gene expression, and overall cellular function [16]. Accordingly, non-physiological oxygen levels distort cellular responses [18] and lead to poorer transferability of results to the human situation. Indeed, physioxia is a key determinant of cellular behavior [17,19]. Crucially, these tissue-specific physioxic levels often lie significantly below atmospheric O_2 concentrations (approx. 21% in air, or 18.5% O_2 under standard incubator conditions), implying that atmospheric conditions in cell culture can themselves represent a hyperoxic state relative to the physiological needs of many cell types [16,17]. For example, it has been shown that physiological hypoxia influences the differentiation of human intestinal epithelial organoids [20]. In that study, however, physioxia was only set by incubator conditions and was not directly measured. It is crucial to critically question whether the set oxygen conditions in the incubator actually reach the cells, or if diffusion limitations and cellular consumption create local microenvironments that significantly differ [21]. While approaches to not only set but also measure physioxia exist [22,23], these methods are often not applicable to every 3D cell culture setup. In this manuscript, our terminology for hypoxia, normoxia, and hyperoxia is consistently applied relative to these established tissue-specific physioxic conditions.

One approach for measuring oxygen in multiple single cancer cell spheroids using sensors in microelectrode wells was demonstrated by Dornhof et al. [24]. They used a bioprinting process to position spheroids directly onto sensors in microwells. Although this represents a first step towards high throughput, oxygen can only be measured at a single point per well. Such electrodes, as developed by Clark [25] or Whalen et al. [26], can measure oxygen precisely, but often not directly in the microenvironment of the cells and thus have limited significance for 3D cell cultures. The development of optical oxygen sensors [27] now enables oxygen to be measured with spatial resolution. The principle is based on dynamic quenching, where oxygen molecules interact with the luminophore, affecting its luminescence properties [28]. A variety of molecules are available for such applications, each with specific advantages and disadvantages [29]. This enables spatially resolved oxygen measurement [30]. The luminophores can be immobilized on films [31,32]. Our combination of such oxygen-sensitive films with a microthermoforming process [33,34] enables the fabrication of oxygen-sensitive microcavities, which we refer to as SensoSpheres [35,36]. With these, spheroids can be generated directly within the microcavities and oxygen can be measured in 3D. To characterize mitochondrial activity more precisely, a so-called 3D mito-stress test was also realized with this system. In this test, mitochondrial respiration was affected by specific inhibitors and the effect on oxygen concentration was determined in 3D for the first time. While previous systems were optimized for 2D cell cultures, this technology offers a solution to fundamental problems in determining physioxia in 3D cell cultures [37].

While our previous work [36] first introduced the basic principle of these O_2-sensitive microcavity arrays as a proof-of-concept, a comprehensive validation, detailed method-

ological optimization, and demonstration of expanded applicability for advanced pharmacological and physiological studies were still lacking.

Building upon this unique technology, this study presents significant advancements that move beyond initial proof-of-concept, substantially expanding its applicability and robustness for advanced research in 3D cell cultures. We introduce optimized protocols for calibration and data analysis and demonstrate the system's versatility by transferring its functionality to standard high-resolution confocal and widefield microscopy platforms, thereby broadening accessibility and utility. Specifically, we establish and characterize hypoxic, hyperoxic, and normoxic conditions and validate the method using various biological models. The platform's enhanced sensitivity and throughput are exemplified by comprehensive substance testing with acetaminophen and cisplatin, utilizing extensive dose–response assays to assess distinct metabolic shifts in spheroids. Furthermore, we introduce the Oxygen Consumption Recovery Rate (OCRR) as a novel quantitative parameter to assess cellular resilience after exposure to toxic compounds. This significantly advanced and high-throughput-compatible platform represents a methodological leap, enabling detailed studies of oxygen-dependent cellular processes, drug toxicity, and metabolic adaptation. Its demonstrated potential for integration into microfluidic systems further paves the way for more sophisticated organ-on-chip models, ultimately improving the predictive power of preclinical research.

2. Materials and Methods

2.1. Sensor and Microcavity Arrays

In this study, various microcavity arrays, including oxygen-sensitive sensor arrays, so-called SensoSpheres, as described by Grün et al., were used [36]. The arrays feature cavities with a diameter of 300 µm and a depth of 350–450 µm (depending on the experiment). Each cavity has a bevel at the upper rim, expanding to 500 µm in diameter, which facilitates the determination of oxygen gradients.

Microcavity arrays were fabricated from polycarbonate films with a thickness of 50 µm (it4ip, Ottignies-Louvain-la-Neuve, Belgium), here referred to as MicroSpheres, and from oxygen-sensitive polymer films (SF-RPC2 or SF-RPC3; PreSens Precision Sensing GmbH, Regensburg, Germany) for SensoSpheres, respectively. For production, a microthermoforming process developed at the Karlsruhe Institute of Technology (KIT, Karlsruhe, Germany) was applied [33–35]. The MicroSpheres or SensoSpheres were bonded to cell culture inserts, developed at KIT and produced by CNC-milling or injection molding.

The work presented here spans several developmental stages of these arrays. In some experiments, the sensor arrays were not yet permanently bonded to an insert but were instead placed into a CellCrown™ insert (Scaffdex, Tampere, Finland) for use in standard 12-well plates. The specific configuration used is indicated in the respective experimental sections.

The sensor arrays (SensoSphere) as well as non-sensor microcavity arrays (MicroSphere) were purchased from CAVIGEN (Karlsruhe, Germany)

2.2. Sterilization, Coating, Handling

CellCrown™ inserts were autoclaved prior to use. SensoSpheres and MicroSpheres can be sterilized using various methods. In these experiments, disinfection with 70% isopropanol, autoclaving (121 °C, 20 min, 3 bar), and a combined protocol involving sodium azide followed by isopropanol treatment were tested. Microcavity arrays and CellCrown™ components were disinfected by immersion in 0.1% sodium azide for two minutes, followed by rinsing in sterile deionized water and a subsequent two-minute immersion in 80% isopropanol. After assembly of the microcavity array into the CellCrown™ insert, the

assembled unit was disinfected again in 80% isopropanol for two minutes. The arrays were then dried under a sterile laminar flow hood and transferred to a 12-well plate for cell culture. Custom-made prototypes (arrays bonded to inserts) were disinfected using the same protocol.

We used BIOFLOAT™ (faCellitate, Mannheim, Germany) coating for spheroid formation. 500 µL of BIOFLOAT™ solution was added to each array and centrifuged at 300× *g* or 1000× *g* for 1 min, depending on the experiment; both variants were tested, but 1000× *g* was used for all subsequent experiments. This ensured uniform coating of the microcavities. After 5 min at room temperature, the coating solution was removed and the inserts were dried for 30 to 60 min under a laminar flow hood. Pre-coated inserts could be stored dry or in $PBS^{(+/+)}$ for several days at 4 °C.

2.3. Cell Culture

Adherent HeLa, HepG2 (ATCC®, Manassas, VA, USA) or HepG2-GFP (INNOPROT, Bizkaia, Spain) cells were cultured in cell culture flasks using HeLa, HepG2 or HepG2-GFP medium under standard conditions (37 °C, 5% CO_2). The culture medium was replaced every three days. Upon reaching an appropriate level of confluence, cells were passaged at ratios ranging from 1:2 to 1:5. The compositions of the media were as follows:

HeLa medium: MEM supplemented with 10% Fetal Calf Serum (7524, Sigma, St. Louis, MO, USA), 1% GlutaMAX™, 1% non-essential amino acids (NEAA), 1% sodium pyruvate, 1% penicillin-streptomycin, and 0.1% phenol red.

HepG2 medium: MEM supplemented with 2.5% human platelet lysate (hPL, ELAREM Perform, PLBioScience GmbH, Aachen, Germany), 1% GlutaMAX™, 1% NEAA, 1% sodium pyruvate, and 1% penicillin–streptomycin.

HepG2-GFP medium: DMEM high glucose supplemented with 10% fetal calf serum (FCS, 30-2020 ATCC®, Manassas, VA, USA) or 2.5% hPL (ELAREM Perform, PLBioScience GmbH, Aachen, Germany), 1% GlutaMAX™, 1% NEAA, 1% sodium pyruvate, 1% penicillin-streptomycin, and 0.5% G418.

Media and supplements were obtained from Thermo Fisher Scientific (Waltham, MA, USA), unless otherwise specified.

2.4. Seeding Cells

For cell seeding, arrays were first filled with cell culture medium by adding 600 µL of medium onto the array, followed by centrifugation at 1000× *g* for 1 min. For CellCrown™ inserts, air bubbles under the array were removed. Subsequently, 400 µL medium was removed, so that only the bottom of the well was covered with medium. Also, cell culture medium on the array was removed. For seeding the appropriate cell number (10^5–10^6 cells), 30 µL medium was added as drops onto the center of the cavities and incubated for 30 min at 37 °C. If assays followed immediately, cell culture medium containing 10 mM HEPES was used. By gravity cells could settle into the cavities. Finally, cell culture medium in the well was increased to 600 µL in the well and 600 µL in the array. Before analysis, cells were incubated for 4 d under standard conditions. For bonded cell culture inserts, cells were directly seeded onto the coated arrays in the appropriate volume.

2.5. Cell Staining Procedures

For live/dead discrimination and spheroid visualization, three different fluorescent dyes were employed: SYTO™16, propidium iodide (PI), and CellTracker™ Green (CTG).

SYTO™16 and Propidium Iodide Staining: SYTO™16 is a cell-permeant nucleic acid dye that selectively stains live cells, while propidium iodide only penetrates cells with compromised membranes, labeling dead cells. For combined live/dead staining, spheroids cultured on arrays were incubated with 5 µM SYTO™16 (prepared by diluting the 1 mM

stock solution 1:200 in cell culture medium) and 3 µM propidium iodide (1:500 dilution from a 1.5 mM stock solution) in cell culture medium, typically overnight at 37 °C. Prior to imaging, the staining solution was replaced with fresh medium.

CellTracker™ Green Staining: For pre-labeling of cells prior to seeding, CellTracker™ Green (CTG) was used. Cells were harvested, centrifuged (300× *g*, 5 min), and resuspended in cell culture medium containing 10 µM CTG (prepared from a 10 mM stock solution in DMSO, diluted 1:1000). The cell suspension was incubated for 30 min at 37 °C, washed with $PBS^{(+/+)}$, and finally resuspended in medium before seeding onto the arrays. Stained cells or spheroids were imaged using fluorescence or confocal microscopy as appropriate for each assay.

Hoechst 33342 Staining: For nuclear counterstaining, Hoechst 33342 was added at a 1:1000 dilution in $PBS^{(+/+)}$ (final concentration of 15 µg/mL) and incubated for 10 min, followed by three $PBS^{(+/+)}$ washes. Imaging was performed using confocal microscopy with excitation at 405 nm (emission 497 nm) for Hoechst and excitation at 480–500 nm (emission 515 nm) for Alexa Fluor® 488.

2.6. Immunofluorescence

HepG2 cells (1×10^5 cells/MicroSphere) were cultured in collagen-coated polycarbonate arrays for five days. After washing twice with 500 µL $PBS^{+/+}$ for 3 min each, cells were fixed with 500 µL Cytofix/Cytoperm™ solution for 30 min at 4 °C and permeabilized with 500 µL Perm/Wash™ buffer (1:10 in ddH_2O) for 15 min at 4 °C. After two additional $PBS^{(+/+)}$ washes, nonspecific binding was blocked with 500 µL of 1% BSA in $PBS^{(+/+)}$ for 1 h at room temperature, followed by three $PBS^{(+/+)}$ washes. The primary antibody (HIF-1α rabbit anti-mouse, 1:100, 2 µM in $PBS^{(+/+)}$ with 0.1% BSA) was added and incubated overnight. After three $PBS^{(+/+)}$ washes, the secondary antibody (Alexa Fluor® 488, 1:200, 0.5 µM in $PBS^{(+/+)}$) was applied for 1 h at room temperature in the dark, followed by three further $PBS^{(+/+)}$ washes.

For pimonidazole staining, BIOFLOAT™-coated arrays were seeded with HepG2 cells (1×10^5 cells/array). On day three, medium volume was adjusted to achieve hyperoxic (800 µL) or hypoxic (3300 µL) conditions. After an additional 24 h, cultures were treated with pimonidazole. A 200 mM stock solution of pimonidazole-hydrochloride (Hydroxyprobe™-1 Kit, Hypoxyprobe, Inc., Burlington, MA, USA) was prepared in $PBS^{(-/-)}$ and stored at 4 °C; a 150 µM working solution in medium was used for staining. Spheroids were incubated with pimonidazole for 24 h, then processed as described for immunofluorescence staining: cells were washed, fixed, permeabilized, and blocked. The primary antibody (Mab1, 1:100 in $PBS^{(+/+)}$, 2 µM, 500 µL) was added, followed by the secondary antibody (Alexa Fluor® 488 goat-anti-mouse, 1:200 in $PBS^{(+/+)}$, 0.5 µM, 500 µL).

2.7. Microscopy

Routine monitoring of cell growth, morphology, and spheroid formation was performed using an inverted light microscope (Axio Vert.A1, Zeiss, Oberkochen, Germany) equipped for phase contrast and fluorescence observation. Imaging was conducted at total magnifications ranging from 50× to 400×, allowing for assessment of both 2D monolayers and 3D structures within the arrays.

For high-resolution imaging and three-dimensional reconstruction, confocal laser scanning microscopy (cLSM) was employed (TCS SP5, Leica Microsystems, Wetzlar, Germany). Confocal microscopy enabled optical sectioning (Z-stacks) through spheroids and microcavities, providing detailed visualization of cellular distribution and spatial organization. Fluorescent dyes were excited with appropriate laser lines (e.g., 405 nm for Hoechst 33342, 488 nm for SYTO™16 and CellTracker™ Green, 514 nm for propidium iodide), and emis-

sion was recorded with an appropriate emission window. Standard acquisition parameters included a pinhole diameter of 70.72 µm, a resolution of 512 × 512 pixels, and a scan rate of 400 Hz. Z-stacks were typically acquired over a depth of 500 µm with a step size of 2–5 µm, depending on the objective and assay requirements.

For additional high-resolution imaging, a Zeiss Axio Observer.Z1/7 inverted microscope (Zeiss, Oberkochen, Germany) was used, equipped with an EC Plan-Neofluar 10×/0.30 M27 objective and an Optovar Tubelens LSM. Three-dimensional data were acquired by capturing Z-stacks consisting of 20 optical sections over a total depth of 380 µm. Excitation was performed using 405 nm and 488 nm laser lines, both at 0.4% power. Images were recorded at a resolution of 1223 × 1098 pixels.

For a comprehensive overview of the microcavities, volumetric imaging was performed using a ZEISS Axio Observer.Z1/7 microscope equipped with the LSM Lightfield 4D module, which enables rapid, single-shot volumetric acquisition. Imaging was conducted with a Plan-Apochromat 20×/0.8 M27 objective. Z-stacks consisting of 99 planes were acquired over a total depth of 428.955 µm at a resolution of 3293 × 3291 pixels. Illumination was provided by a 385 nm LED module at 1.1% intensity with an exposure time of 10 ms, resulting in a depth of field of 1.45 mm.

2.8. Adjustment of O_2-Concentrations—Hypoxia, Hyperoxia and Normoxia

Oxygen levels in the microenvironment of 3D cell cultures were controlled by varying the height of the culture medium above the microcavity arrays. To establish hypoxic, normoxic, or hyperoxic conditions, the total volume of medium in the well was adjusted, thereby altering the diffusion path for atmospheric oxygen to reach the cells. Our definitions of hypoxic, normoxic, and hyperoxic conditions in this study are based on their relation to the physioxic oxygen levels of human liver tissue (typically 4–7% O_2) [17,38,39].

For hypoxic conditions, the medium volume was increased (up to 2.55 mL per array), resulting in a longer diffusion distance and reduced oxygen availability within the microcavities. Normoxic oxygen concentrations were achieved by using intermediate medium volumes (typically 0.55 mL in the inner area of the cell culture inserts) leading to oxygen saturations that stabilized between 4% and 7%, whereas hyperoxic conditions were set by minimizing the medium volume (as low as 0.1 mL per array), yielding oxygen concentrations close to atmospheric levels, which are considered hyperoxic for liver cells due to significantly exceeding their physiological range.

Oxygen concentrations in the direct vicinity of the spheroids were continuously monitored in real time using SensoSpheres. Sensor readouts allowed precise quantification and validation of the established oxygenation states. This approach enabled the reproducible adjustment of oxygen levels in 3D cultures without the need for specialized gas controllers or hypoxia chambers.

2.9. Oxygen Sensing and Calibration

2.9.1. Oxygen Measurement Using VisiSens TD/MicrosCubes (PreSens GmbH)

For oxygen measurements in multiple microcavities, we used the VisiSens TD and MicrosCube systems (PreSens Precision Sensing GmbH, Regensburg, Germany), which fit into a standard incubator and enable long-term monitoring. The MicrosCube utilizes dynamic fluorescence quenching and ratiometric detection with a blue LED-excited oxygen-sensitive fluorophore (em. 630–670 nm) and a reference fluorophore (em. 490–550 nm) integrated in the SensoSpheres. For calibration, a two-point protocol with 100% air saturated water and 0% oxygen was applied: 1 mL dH_2O was added to the array, centrifuged at 1000× *g* for 1 min to remove air bubbles, and equilibrated for 5–15 min to define the 100% (a.s.) oxygen value (R100). After equilibrium, 600 µL of freshly prepared 20 mg/mL Na_2SO_3 solution

was added to achieve 0% oxygen (R0) after approximately five minutes. Measurements were performed at 2 min intervals, with gain set to 10 and exposure time optimized (1–2 s). For long-term experiments, time-lapse imaging was conducted at 30 min intervals.

2.9.2. Oxygen Measurement Using cLSM

Oxygen measurements were performed using the SP5 confocal microscope (Leica Microsystems) or the Axio Observer.Z1/7 (Zeiss). HepG2 and HepG2-GFP cells were seeded at densities of 5×10^4, 1×10^5, or 5×10^5 cells per array and cultured for 4 days. Imaging with the SP5 was conducted with a 10× objective (HC PL FLUOTAR 10.0 × 0.30 DRY) due to working distance constraints. Excitation was provided by a 405 nm diode laser at 10–30% intensity, with gain and offset individually adjusted for each image. Standard acquisition parameters included a pinhole diameter of 70.72 µm, a resolution of 512 × 512 pixels, and a scan rate of 400 Hz. Z-stacks were acquired over a depth of 500 µm with a step size of 5 µm.

For calibration, 600 µL dH_2O was added to the well and 300 µL dH_2O to the array (in CellCrown™ inserts), followed by centrifugation at 1000× *g* for 1 min to remove air bubbles. For 100% oxygen calibration, images were taken every 2 min over 30 min. For 0% oxygen calibration, 600 µL of 20 mg/mL Na_2SO_3 was added and images were again acquired every 2 min for 30 min. Different calibration media, including HEPES-buffered medium (10 mM) and water, were tested to optimize measurement conditions.

2.9.3. THUNDER Imager from Leica

Oxygen measurements using the Thunder Imager (Leica Microsystems) were performed with a calibration protocol analogous to that of the SP5 confocal microscope. Measurements were acquired every minute for five minutes. Imaging was conducted with both 10× (HC PL FLUOTAR 10×/0.32 DRY) and 5× (N PLAN 5×/0.12 DRY) objectives, using the DFT51010 filter cube (Leica Microsystems, Wetzlar, Germany) (emission: 535 nm for the reference fluorophore, 642 nm for the sensor fluorophore). Excitation was provided at 390 nm with an LED intensity of 3%, and exposure times were adjusted as needed. The transmitted light channel was set to 100%. The Thunder system utilizes widefield illumination with computational clearing to remove out-of-focus light, enabling rapid Z-stack acquisition and high-contrast 3D imaging of the microcavity arrays.

2.10. Image Analysis

For quantitative analysis of oxygen measurements, four different software tools were tested: MITOS-plugin VisiSens Scientifical 1.0.3.2 (PreSens Precision Sensing GmbH, Regensburg, Germany), CellProfiler™ 4.2.7 (Broad Institute, Cambridge, MA, USA), ImageJ Fiji 2.9.0 (Open Source, Bethesda, MD, USA), and a custom Python 3.13.3 (Python Software Foundation, Wilmington, DE, USA) script. Since no single software solution fully met the requirements for evaluating these datasets, each tool was assessed and optimized for specific aspects of image and data analysis.

2.10.1. MITOS-Software, PreSens

For rapid initial assessment of oxygen measurements, the MITOS software plugin (PreSens) was employed. This tool allowed real-time visualization and quantification of oxygen levels by defining regions of interest (ROIs) within the microcavity arrays and tracking fluorescence intensity changes over time. The software facilitated efficient evaluation of measurement quality and identification of equilibrium points for calibration. However, for normalization purposes, an Excel macro was used. This macro detected the size of the data sheet, calculated the mean fluorescence intensities of the bevel and the

microcavity over time, normalized the data to the maximum values usually determined after NaN_3 administration, and finally displayed the oxygen concentrations in a line graph.

2.10.2. CellProfiler™

Image analysis of oxygen measurements was performed using the open-source software CellProfiler™ according to [35]. A custom pipeline was developed to automatically identify microcavities as objects, segment them into distinct regions (region of interest, ROI: spheroid, inner and outer bevel), and calculate intensity ratios (R-values) between the oxygen-sensitive (red) and reference (green) fluorophores. The resulting R-values were exported as .csv files and further processed in Excel. Oxygen concentrations were calculated using the two-point calibration, the material factor (A = 0.82), and the modified Stern-Volmer equation. In cases where some cavities were not detected due to imaging artifacts, the mean of all identified cavities was used for analysis.

Stern-Volmer equation

$$p_{O_2} = \frac{R_0 - R}{K_{SV} * ((A-1) * R_0 + R)}, \quad (1)$$

2.10.3. ImageJ

Image analysis with ImageJ (Fiji) involved loading 3D image stacks and manually placing regions of interest (ROIs) over the areas corresponding to the microcavities. These ROIs were then transferred to the other fluorescence channel to ensure identical regions were analyzed for both the oxygen-sensitive and reference signals. Using the ROI Manager and Measure tools, intensity values for up to seven cavities per image (at 10× magnification) were extracted across all Z-slices and time points. The resulting data were exported to Excel for further processing and calculation of oxygen concentrations.

2.10.4. Python Script/Visual Studio Code

A custom Python script, developed in Visual Studio Code, v1.108.x, was used for automated analysis of 3D microscopy images from oxygen measurements. The script processed image stacks from both red (oxygen-sensitive) and green (reference) fluorescence channels. Users specified the number of time points and Z-slices to be analyzed, as well as intensity thresholds for each channel to distinguish relevant signal from background. The script filtered out slices without sufficient signal, calculated mean intensities for each channel, and generated R-values (red/green ratio) for all images. Results were exported as Excel files for further quantitative analysis.

2.11. Statistical Analysis

For statistical analysis, either the Mann–Whitney U-test or the t-test was applied as appropriate. For calibration experiments, normality was assessed using the Shapiro–Wilk test (Cube 1: n = 31, Cube 2: n = 28; significance level p = 0.05). If $p > 0.05$, data were considered normally distributed and analyzed using the t-test; otherwise, the Mann–Whitney U-test was used.

2.12. Dose–Response Assay with Acetominophen and Cisplatin

To characterize the influence of cisplatin (CP) and acetaminophen (APAP) on mitochondrial respiration of spheroids, dose–response assays with increasing concentrations were performed [40,41]. Spheroids were pre-cultured for two days prior to substance exposure. For CP, a 1 mM stock solution was initially prepared in $PBS^{(+/+)}$, but was later switched to 0.9% NaCl to improve compound stability and compatibility. In the initial protocol, HeLa spheroids were treated with stepwise additions of CP at concentrations of 3,

10, 20, 40, and 80 µM (each added at 60 min intervals), followed by higher concentrations of 80, 160, 240, and 320 µM. Based on these results, the effective dose range for HeLa was narrowed to 40–160 µM, and subsequent experiments used single-dose additions without stepwise increases. For HepG2 spheroids, only a single dose of 10 µM CP was applied due to higher sensitivity. In a later protocol, the dose range was further expanded to include 3.5, 7, 14, 50, 100, 200, 400, and 800 µM CP.

APAP was tested analogously, with a 100 mM stock solution first prepared in DMSO and then diluted to 10 mM in $PBS^{(+/+)}$ to avoid DMSO-related artifacts. Dose ranges from 5 to 320 µM were evaluated, with initial stepwise additions and subsequent focus on single doses of 40, 80, and 160 µM for both HeLa and HepG2 spheroids. In a later approach, APAP was directly prepared in $PBS^{(+/+)}$ and tested at concentrations of 70, 140, and 280 µM.

For all dose–response assays, substances were added directly to both the cell culture insert and the surrounding well, and oxygen consumption was monitored in real time using the established 3D Mito-Stress Test protocol. The timing and concentration of each addition, as well as the resulting changes in oxygen saturation, were recorded and analyzed.

2.13. Oxygen Consumption Recovery Rate (OCRR)

For the determination of the oxygen consumption recovery rate, a numerical differentiation of the results graphs was performed. Peak values from the graphs were differentiated according the following formula:

$$OCRR = \frac{1}{h}\left(\frac{y_{i+1} - y_i}{h} - \frac{y_i - y_{i-1}}{h}\right) [\%/\text{min}]$$

where

h = measuring interval in [min] and
y = measured peak oxygen concentration after administration of the medium or the respective drug concentration at timepoint peak (i), 1 min later (y_{i+1}) or 1 min prior to (y_{i-1}) in [%]

2.14. Microfluidic Devices

2.14.1. Development of Microfluidic Platforms—The OxyFloat Platform

To enable experiments with 3D cell cultures, two microfluidic platform concepts were developed. The following requirements for dynamic cell culture with microcavity arrays were identified and defined as a specification sheet: (i) reliable inoculation of microcavity arrays; (ii) controlled gas exchange to allow for hypoxic conditions; (iii) photometric oxygen measurement at the reactor; (iv) medium recirculation using a single micropump; (v) inlet and outlet ports for medium exchange and cleaning; (vi) access for substance addition; and (vii) biocompatibility of all materials in contact with the culture medium (Figure 1). The platform was to operate with only one pump, capable of manipulating small flow rates (0–1000 µL/min) and integrating into a process control or automation system. Switching between operational modes required the use of valves. For oxygen measurement, the microcavity array with the cell culture had to remain accessible for optical detection. The design also considered compatibility with the MicrosCube system already in use for optical oxygen measurements, as well as minimizing dead volume in tubing and components to reduce reagent consumption.

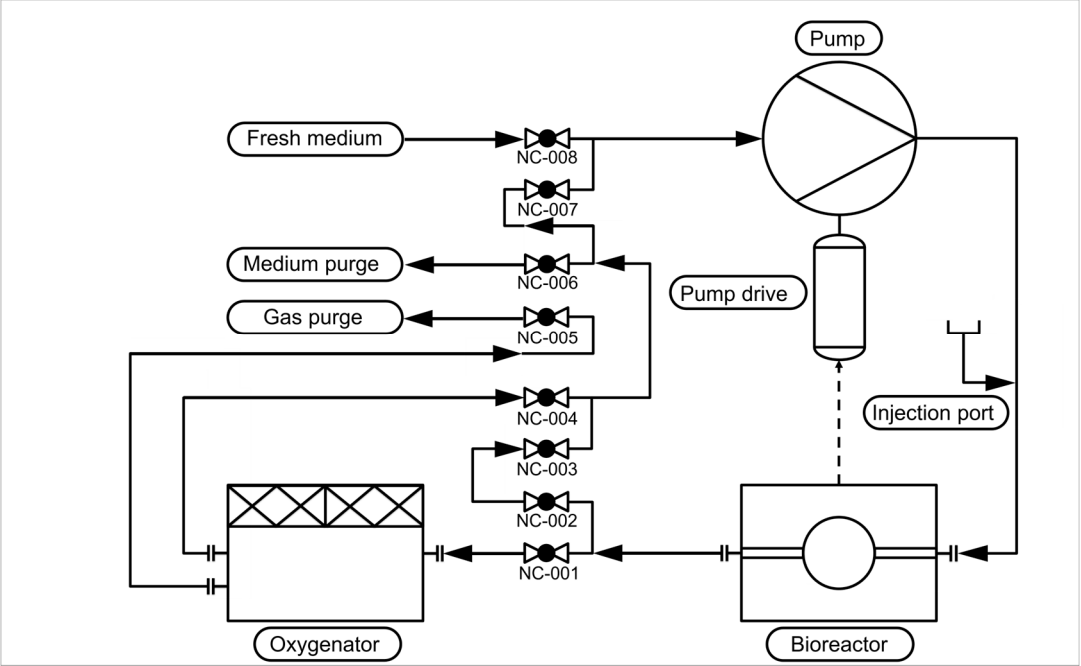

Figure 1. Refined base flow diagram for defining operating modes with 2-way valves. The schematic shows the principal components and flow paths used to control medium delivery and gas exchange for microcavity-array reactors, including a single micropump (Pump), a microreactor containing the microcavity array (Bioreactor), an oxygenator with gas-exchange membrane, an injection port, a series of normally closed 2-way valves (NC-001 to NC-008) and fresh medium/purge reservoirs depicted as inlet and outlet streams. Arrows indicate the primary pump flow direction; valve states are used to configure distinct operational modes while minimizing dead volume and branch length to enable rapid switching and reproducible perfusion. Based on this layout, the following operating modes were implemented: (1) recirculation through all modules (full-circuit mode); (2) recirculation with the oxygenator bypassed (oxygenator bypass/hypoxia induction); (3) flush/medium exchange; (4) flush/medium exchange with the oxygenator bypassed. This diagram serves as the reference layout for the valve-state table used to operate and automate experiments.

2.14.2. Additive Manufacturing

Two additive manufacturing techniques were employed for the fabrication of microfluidic device components: filament-based 3D printing and photopolymer 3D printing. For initial prototypes and less geometrically complex microfluidic parts, fused deposition modeling (FDM) was performed using a Bambu Lab P1P (Bambu Lab, Shenzen, China) printer with 1.75 mm PETG filament. Printing was conducted with a layer thickness of 0.2 mm, a heated bed temperature of 70 °C, and a nozzle temperature of 220 °C. To minimize warping, a rubber-coated anti-warp build plate and a PMMA enclosure for thermal stability were used.

For microfluidic components requiring higher resolution and removable support structures, photopolymer 3D printing was performed on a Stratasys Objet260 Connex3 (Stratasys, Eden Prairie, MN, USA) using Veroclear resin and SUP705 support material (Stratasys, Eden Prairie, MN, USA). Support removal was achieved by etching in 2 M sodium hydroxide for 1–4 days, followed by mechanical cleaning with plastic brushes of varying hardness. Residual support material at critical sealing surfaces and tight tolerances was removed with spatulas and flat screwdrivers as needed.

2.14.3. Protocol to Set-Up the Microfluidic Platform

Prior to use, the empty microcavity array was sterilized and assembled into the reactor [35]. The reservoir was initially filled with deionized water, and the system was

primed in the pump's flow direction via the inlet line using a pipette. The pump was set to maximum output, and all valves were sequentially actuated to verify their function and to remove air bubbles through the waste line. The system was operated for 2 h under alternating flow modes to confirm leak-tightness. Following successful testing, the pump flow rate was calibrated to 400 µL/min by adjusting the voltage at a set frequency (typically 300 Hz and 150 V for the OxyFloat platform) while measuring the displaced water volume over 5 min.

For disinfection, the reservoir was filled with 10 mL of 0.1% sodium azide and all lines were flushed for 30 min under varying flow conditions. The system was then rinsed with deionized water, which was replaced once during the process. Next, the reservoir was filled with 10 mL of complete cell culture medium and the system was flushed to remove residual water, ensuring no backflow into the reservoir. For inoculation, the reactor lid was removed, and the empty microcavity array was replaced with a pre-seeded array. The reactor was resealed and the circulation restarted, allowing the reactor to fill and remaining air bubbles to be purged before commencing the experiment.

3. Results

3.1. System Development and Protocol Optimization

During these experiments, we used microcavity arrays placed in commercially available CellCrown™ inserts. However, leakage at the insert screw connections required relatively high medium volumes. To address this, we advanced the technology by laser-welding the microcavity films directly onto CellCrown™ frames (Telproekta EOOD, Bulgaria; microfluidic ChipShop, Jena, Germany). This also enabled the design of customized inserts for 12-well plates with either one or four compartments, initially fabricated by 3D printing (Veroclear). In the next stage, inserts were manufactured from polycarbonate via machining, and an injection-molded variant was produced (Figure 2a). For these, ultrasonic welding (Herrmann Ultraschall, Karlsbad, Germany) was tested as a bonding technique. The thermoforming process for these arrays utilizes optimized brass molds featuring microcavities with a 300 µm diameter and a bevel. While molds with both 30° and 60° bevels were used in our experiments, we here exemplarily show a mold with a 30° bevel, which facilitates the creation of oxygen gradients (Figure 2b,c). The resulting microcavity arrays were characterized using digital microscopy to confirm the profile and dimensions of the replicated structures (Figure 2d,e).

Previously, sterilization was mainly performed with isopropanol, which proved unreliable. Autoclaving was also tested, but this resulted in a marked reduction in the intensity of the oxygen-sensitive fluorophore. The best results were achieved with a combined sodium azide and isopropanol protocol.

To maximize cell yield and minimize losses during seeding in CellCrown™ inserts, the protocol was optimized to include a centrifugation step; for welded inserts, this step was less critical due to improved retention. Overall, these developments led to improved system tightness, reduced medium consumption, and more robust and reproducible cell seeding.

As a proof-of-concept for the optimized system, HepG2-GFP cells were successfully cultured, forming uniform spheroids as visualized by fluorescence microscopy (Figure 2f,g). Particularly promising for future high-throughput applications is the use of ZEISS LSM Lightfield 4D imaging (Figure 2h), which allows for instantaneous, high-speed volumetric imaging of entire microcavity fields. This technology, capable of capturing up to 80 volumes per second with minimal phototoxicity, could be adapted for rapid, parallelized 3D oxygen measurements, significantly increasing the throughput of metabolic and toxicological screenings.

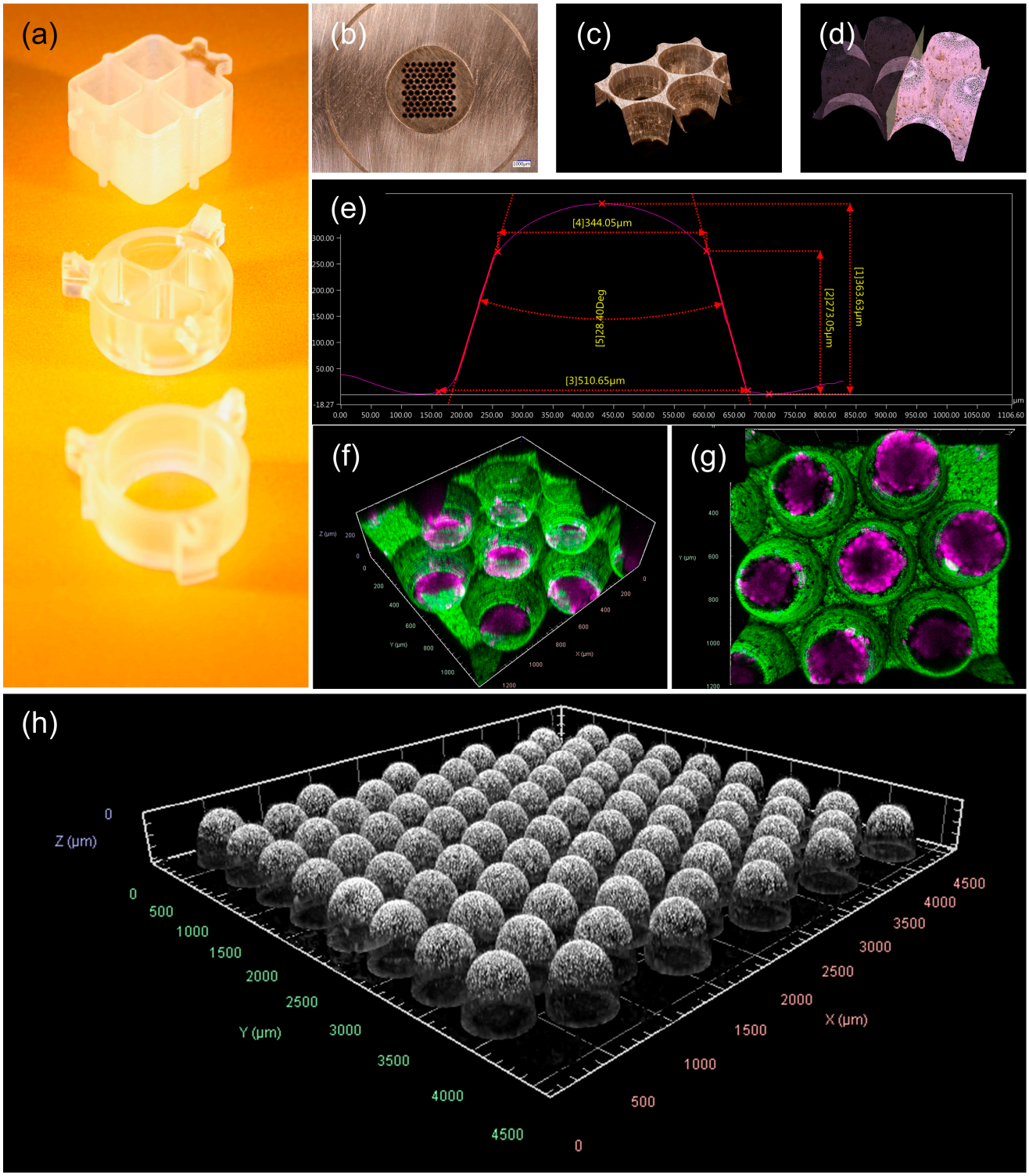

Figure 2. Fabrication and application of microcavity sensor arrays (SensoSpheres). (**a**) Prototypes of custom cell culture inserts designed for 12-well plates. (**b**) The brass mold insert used for thermoforming, featuring microcavities with a 300 µm diameter and a 30° bevel. (**c**) Detailed micrograph of a milled bevel on the mold insert. (**d**) Micrograph of a thermoformed sensor array replicated from an SF-RPC3 film. (**e**) Dimensional analysis of the replicated microcavity, confirming its depth and profile. (**f**,**g**) Fluorescence microscopy images using the Zeiss LSM Axio Observer of HepG2 spheroids cultured within the SensoSpheres. Nuclei are stained with Hoechst 33342 (pseudocolored magenta for visualization). The green signal originates from the SF-RPC3 sensor foil's green reference fluorophore, (**h**) shows an overview of the microcavities using the Zeiss Lightfield 4D.

3.2. Calibration

Various calibration methods were tested, including adjustments of sample volumes and comparisons between calibrations performed in water and in cell culture medium.

The two-point calibration protocol using dH_2O and Na_2SO_3 proved robust and reproducible for the SensoSpheres. The protocol workflow is illustrated in Figure 3. Optimal calibration required a minimum liquid volume of 300 µL (dH_2O or Na_2SO_3 solution) in the insert and 600 µL in the surrounding well. Lower volumes led to instability and unreliable R_0 values, mainly due to leakage in the CellCrown™ inserts. No significant differences in calibration values were observed before and after coating or cell culture, indicating stable sensor performance. Calibration in cell culture medium resulted in lower and less stable R_0 values compared to dH_2O; therefore, dH_2O was preferred for routine calibration.

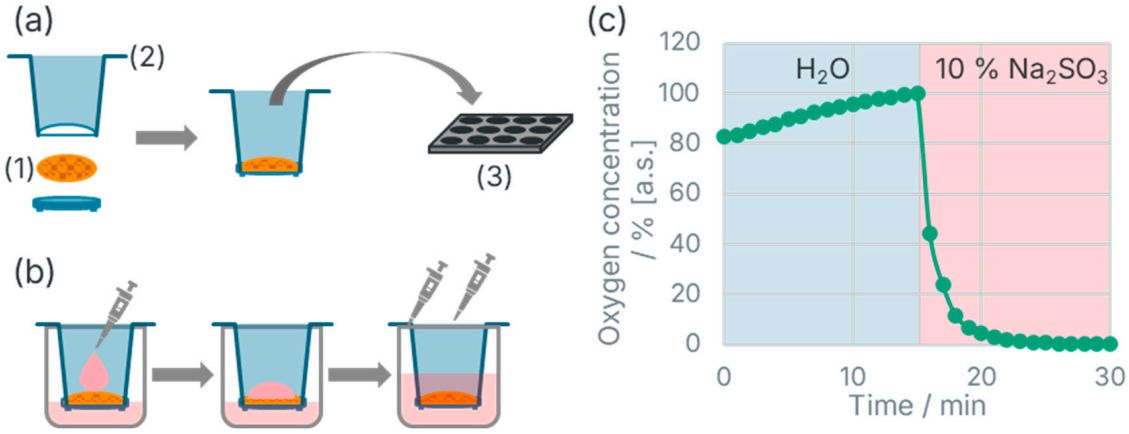

Figure 3. Optimized protocols for working with MicroSpheres and SensoSpheres in CellCrown™ inserts. (**a**) Schematic workflow illustrating the integration of the microcavity array (1), MicroSphere or SensoSphere, into the CellCrown™ insert (2) and a 12-well plate (3). (**b**) Workflow for cell seeding according to the optimized protocol. In brief, cells are carefully placed in an adequate volume in the center of the microcavity array, allowed to settle into the cavities by gravity, and after an initial incubation period, cell culture medium (light red) is added into the insert and the surrounding well according to the experimental design. (**c**) Representative calibration measurement for oxygen sensing. The green line with green dots depicts the oxygen concentration (a.s.) over time. The initial phase (0–15 min) represents the measurement of water (dH_2O) for the R100 calibration point, followed by the addition of 10% Na_2SO_3 solution (after 15 min) to establish the R0 calibration point (0% oxygen).

The average R_0 (0% oxygen) values were approximately 1.40 (Cube 1) and 1.43 (Cube 2), while the average R_{100} (100% oxygen) values were 0.76 (Cube 1) and 0.70 (Cube 2). R_0 and R_{100} values within each device differed significantly, confirming effective calibration. R_0 values were comparable between devices, but R_{100} values showed a significant difference, indicating the need for separate calibration for each device.

3.3. Oxygen Measurement Using Microscopes

Initially, oxygen measurements were performed exclusively with the VisiSens TD and MicrosCube devices of PreSens. However, as the fluorescence emission spectra of the sensor arrays were within the standard range, transferring the method to other fluorescence microscopes was a logical next step. The use of confocal microscopy (cLSM, Leica SP5 and SP8) was expected to provide higher Z-resolution and more detailed three-dimensional imaging. Therefore, the measurement protocol was adapted for the Leica SP5 and SP8 and further compared to the faster Leica THUNDER Imager. The emission maxima of the reference and oxygen-sensitive fluorophores were confirmed by lambda scans: with 405 nm excitation (SP5/SP8), the reference fluorophore peaked at 500–510 nm and the

oxygen-sensitive fluorophore at 650–660 nm; for the THUNDER Imager, excitation was at 390 nm (Figure 4).

For oxygen measurements, the calibration protocol was adapted for each microscope. When calibrating with dH_2O, the mean R-values for R100 and R0 were 0.47 and 1.00, respectively, resulting in a difference of 0.53. In contrast, calibration with HepG2 complete medium produced mean R-values of 0.53 (R100) and 0.71 (R0), yielding a smaller range of 0.18. These findings indicate that dH_2O as a calibration medium provides a larger dynamic range between 0% and 100% oxygen, which may be advantageous for subsequent cell measurements. For the THUNDER Imager, no significant difference was observed in the distribution of R-values between dH_2O and HepG2 medium calibrations; however, calibrations on the SP5 showed greater variability and less consistency. A statistically significant difference between R100 and R0 was observed for calibrations in HepG2 medium on the THUNDER Imager (Figure 5).

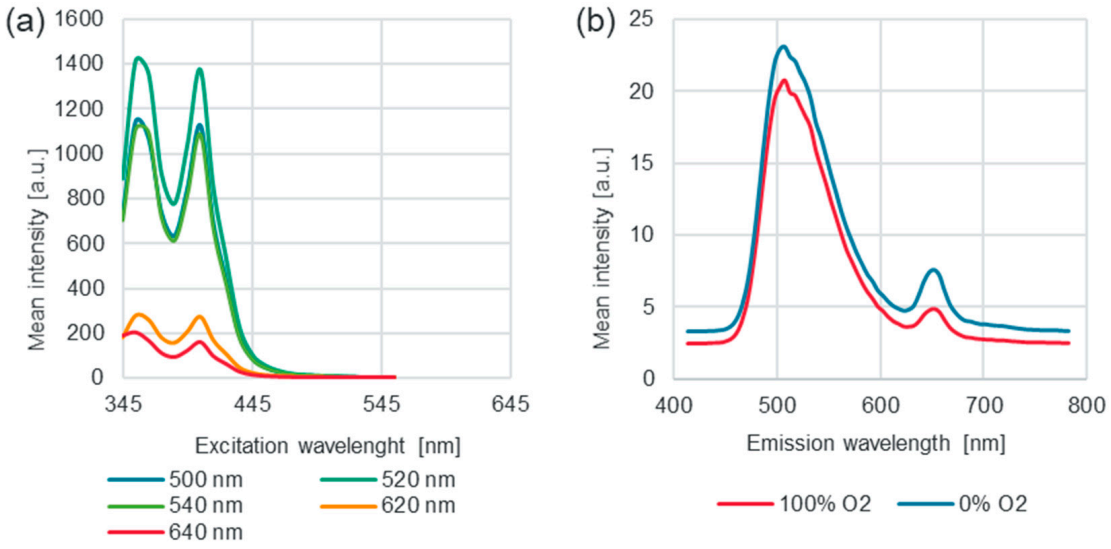

Figure 4. Emission and excitation scan. (**a**) Excitation scan reveals two excitation peaks at 355 nm and 405 nm by using 517 nm as an emission setting. The scan was performed using the two-photon SP8 microscope from Leica over an excitation range of 345 nm to 555 nm, with an emission wavelength range of 500 nm to 690 nm (only relevant emission wavelengths are represented; 500 nm (teal blue), 520 nm (emerald green), 540 nm (moss green), 620 nm (orange) and 640 nm (red)). The *x*-axis represents the excitation wavelength in nm, the *y*-axis represents the mean intensity in arbitrary units [a.u.]. Intensity values were analyzed using ImageJ; Microscopy settings: laser = Argon (28.57%), scan speed = 100 Hz, objective = HC PL APO 10×/0.40 DRY. (**b**) Emission scan acquired with 405 nm excitation was performed for water saturated with oxygen (dH_2O, ambient atmospheric pO_2, 100% O_2 a.s.) and 0% oxygen (by adding 20 mg/mL Na_2SO_3 solution). The scan was performed using Leica SP5 confocal microscope over an emission range of 410 nm to 780 nm. The *x*-axis represents the emission wavelength in nm, the *y*-axis represents the mean intensity in arbitrary units [a.u.]. Intensity values were analyzed using ImageJ; Microscopy settings: laser = UV diode (30%), scan speed = 400 Hz, objective = HC PL APO 10×/0.40 DRY.

In summary, oxygen measurements could be performed with SP5, SP8 and THUNDER microscopes, but the THUNDER Imager provided more robust, rapid, and reproducible results. The greater consistency and dynamic range of the THUNDER Imager, along with its faster acquisition and computational clearing, make it better suited for high-throughput and quantitative oxygen measurements in 3D cell culture systems.

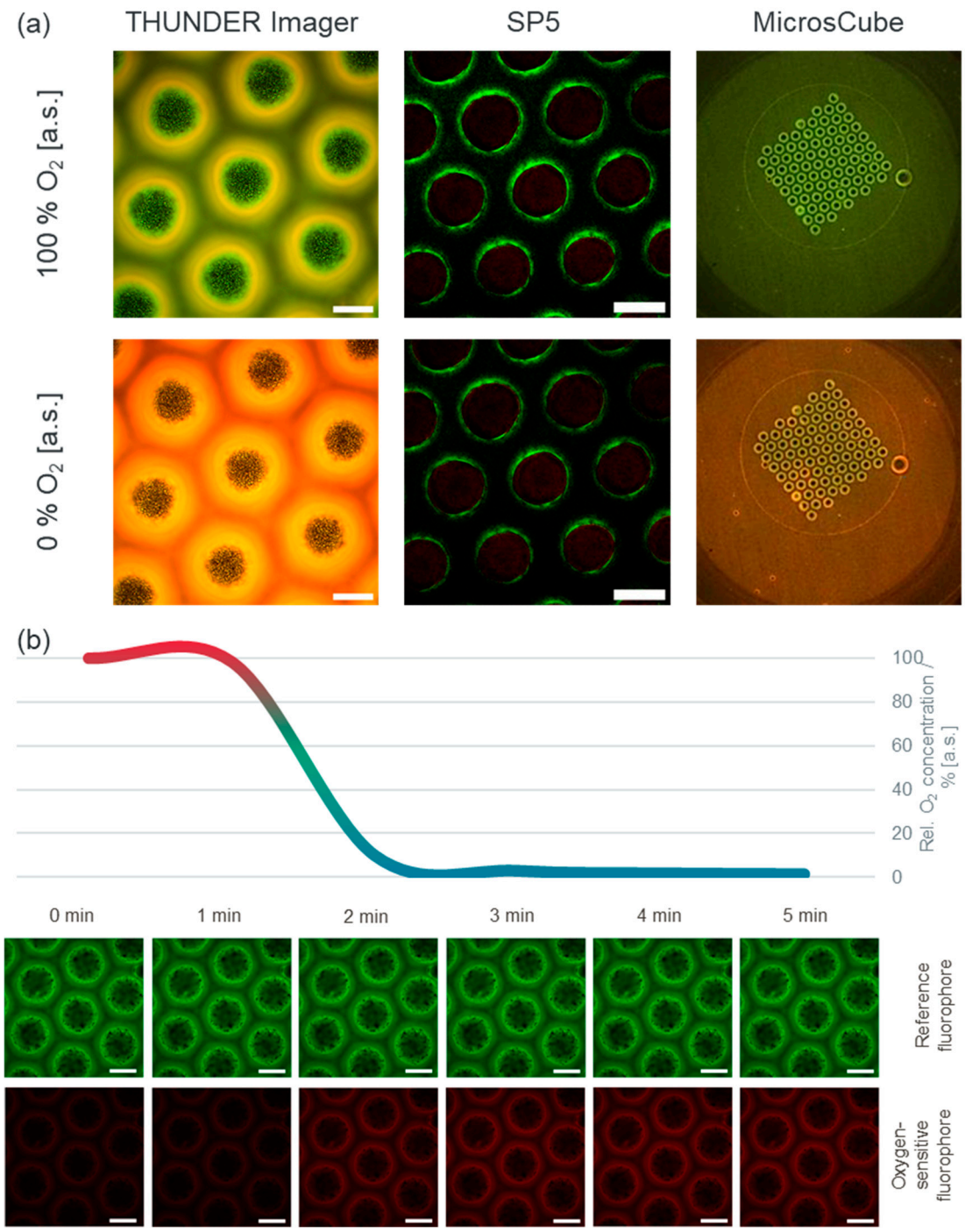

Figure 5. (**a**) Visual representation of dynamic quenching effect by oxygen. Acquired with THUNDER Imager, SP5 (Leica) and the MicrosCube (PreSens). Merged images show increased fluorescence intensity at 0% oxygen, except for SP5. THUNDER Imager/SP5 scale bar = 200 µm. The MicrosCube image, included to illustrate the methodological principle of oxygen sensing, does not generate scale bars as its primary function is quantitative oxygen measurement rather than high-resolution microscopy; hence, its field of view is not directly comparable in scale to the other systems. In the microscopic images, a higher proportion of red fluorescence appears as an orange hue, indicating a reduction of the quenching effect by oxygen and thus representing lower oxygen concentrations. (**b**) Calibrations performed with THUNDER Imager. Calibration of RPC2 sensor array with dH_2O demonstrates the direct effect of dynamic quenching on relative oxygen concentration. The time-lapse images show the increase in fluorescence of the oxygen-sensitive fluorophore and the stable intensity of the reference fluorophore. Oxygen concentration is represented by a color gradient along the line, shifting from red (high O_2) to blue (low O_2). Scale bar = 200 µm; analyzed with Visual Studio Code.

3.4. Hypoxia, Hyperoxia, and Normoxia

Using SensoSpheres (oxygen-sensitive microcavity arrays), HepG2 spheroids were cultured under defined oxygen conditions by varying the medium volume in the wells. Hypoxic conditions were established with 3250 µL medium (2550 µL within the array), resulting in a rapid decrease in oxygen saturation to below 20% within six hours and stabilizing just above 0% after 20 h. Normoxic conditions were maintained with a medium volume of 1200 µL (600 µL within the array), leading to oxygen saturations that stabilized between 10% and 20% over 20 h. Hyperoxic conditions were achieved by reducing the total medium volume to 800 µL (resulting in 100 µL within the insert), resulting in oxygen saturation values rising above 40% after four hours and remaining relatively constant thereafter (Figure 6a). These oxygen levels were confirmed in three independent experiments. The protocol enabled stable oxygen environments for up to 48 h, supporting both long-term culture and downstream analyses (Figure 6b).

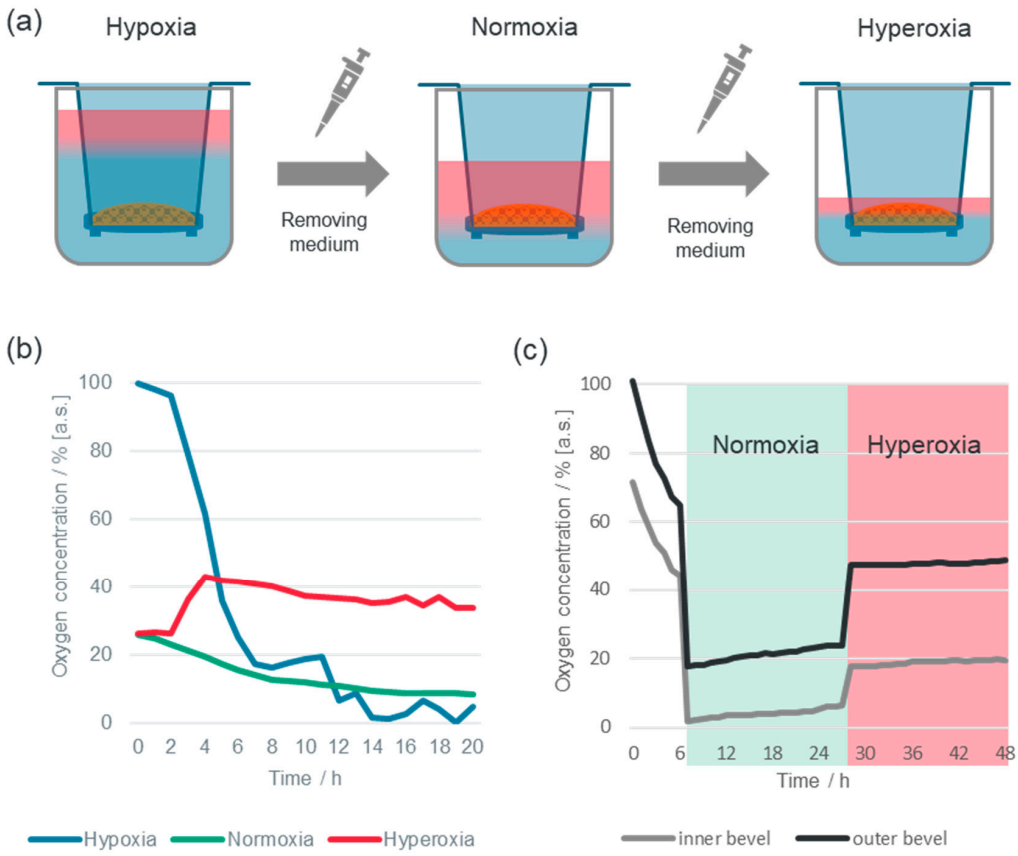

Figure 6. Oxygen concentrations during cultivation of HepG2 spheroids under hyperoxic, normoxic and hypoxic conditions. (**a**) Schematic illustration depicting the adjustment of medium filling heights (e.g., by removing medium with a pipette) which influences oxygen diffusion and consequently leads to hypoxic, normoxic, and hyperoxic conditions. The gradient in the figure displays decreasing oxygen concentration, transitioning from red (high) to blue (low). (**b**) Time course of oxygen concentration changes over 20 h under hypoxia, normoxia and hyperoxia. (**c**) Oxygen gradient formation comparing an upper region at the cavity bevel (outer bevel) and a deeper region adjacent to the spheroids (inner bevel). After seeding, cultures were maintained under hypoxic conditions; the high initial saturation reflects the large medium volume. Normoxic conditions were applied after 6 h and hyperoxic conditions after 26 h.

Immunofluorescence staining for hypoxia markers HIF-1α and pimonidazole demonstrated clear, condition-dependent responses in HepG2 spheroids (Figure 7). After four days of culture and subsequent exposure to hypoxic, normoxic, or hyperoxic conditions, strong

green fluorescence for HIF-1α and pimonidazole was observed in spheroids under hypoxia, particularly at the periphery, indicating activation of hypoxia response pathways and protein modifications specific to low oxygen. In normoxic spheroids, only weak green fluorescence was detected, while under hyperoxic conditions, essentially no green fluorescence was present. These patterns were consistent across multiple Z-stack layers in confocal microscopy. The results confirm that the system induces and detects robust molecular signatures of hypoxia and hyperoxia, validating the use of these arrays and staining protocols for studying cellular adaptation and oxygen-dependent signaling in 3D liver spheroids.

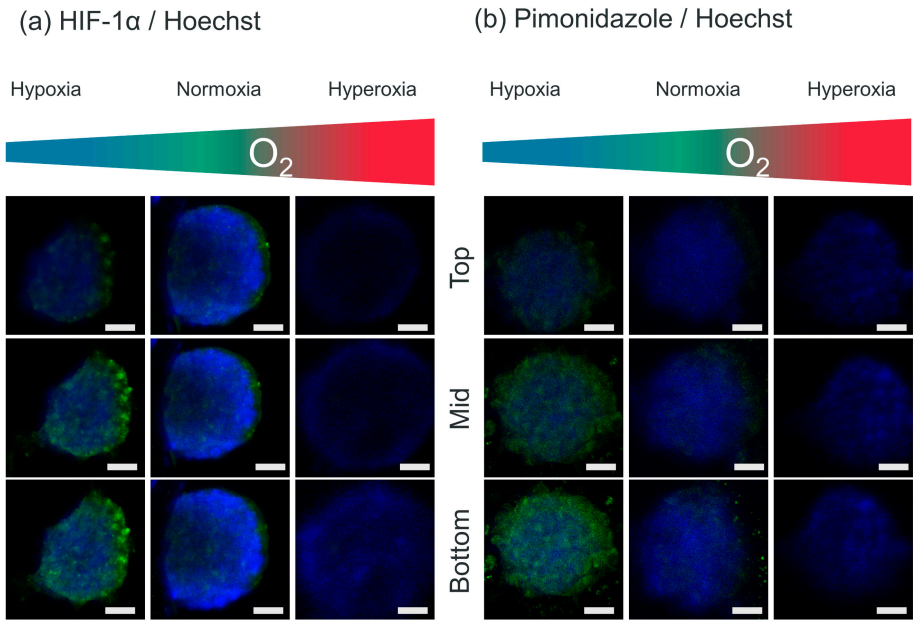

Figure 7. Representative Z-plane images of indirect immunofluorescence staining for hypoxia in HepG2 spheroids (1×10^5 cells/array) after 4 days of culture and 24 h exposure to adjusted medium heights. For each condition (hypoxic, normoxic, hyperoxic), three representative Z-planes are shown: Top, Mid, and Bottom. (**a**) HIF-1α staining (green) with Hoechst 33342 nuclear counterstain (blue). (**b**) Pimonidazole adduct staining (green) with Hoechst 33342 (blue). Under hypoxic conditions, spheroids display strong cytoplasmic/peripheral green signal for both markers, which varies across the Z-planes, consistent with internal gradients. Normoxic spheroids show only weak green signal, predominantly in the mid-plane, while hyperoxic spheroids exhibit no detectable green signal throughout. This multi-plane representation demonstrates the marker changes with hypoxia across the spheroid's depth. Scale bar = 70 μm.

3.5. Acetaminophen and Cisplating Testing in Spheroids Using Dose–Response Assays

Dose–response experiments with cisplatin and acetaminophen (APAP) revealed a clear, concentration-dependent inhibition of mitochondrial respiration in both HeLa and HepG2 spheroids. In HeLa spheroids, cisplatin at concentrations of 80 μM and above led to a pronounced and sustained increase in oxygen saturation, indicating strong inhibition of the respiratory chain. APAP produced a similar effect at concentrations of 80 μM and higher, though the kinetics differed from those of cisplatin. In HepG2 spheroids, even lower doses of cisplatin (as low as 3–10 μM) resulted in a noticeable inhibition of respiration, while APAP effects were weaker and often reversible at lower doses. In some experiments, especially at higher doses or after repeated additions, cell viability was compromised, resulting in a lack of further response to test substances.

In subsequent experiments, the dose ranges for both cisplatin and acetaminophen were further expanded and refined (Figure 8). Testing lower cisplatin concentrations (3.5, 7, and 14 μM) confirmed that HepG2 spheroids are highly sensitive, with clear inhibition of mitochondrial respiration observed even at these low doses. At higher concentrations (up

to 800 µM), both HepG2 and HeLa spheroids exhibited a rapid and sustained increase in oxygen saturation, consistent with strong mitochondrial inhibition and eventual cell death. For acetaminophen, the use of DMSO as a solvent initially affected the results, but switching to $PBS^{+/+}$ for stock solution preparation improved assay reliability. At concentrations of 70 µM and above, APAP induced dose-dependent mitochondrial inhibition, though the extent and kinetics of the response varied between cell lines and experimental conditions. These results further highlight the importance of careful dose selection, solvent choice, and spheroid quality for achieving reproducible and interpretable outcomes in 3D Mito-Stress Tests.

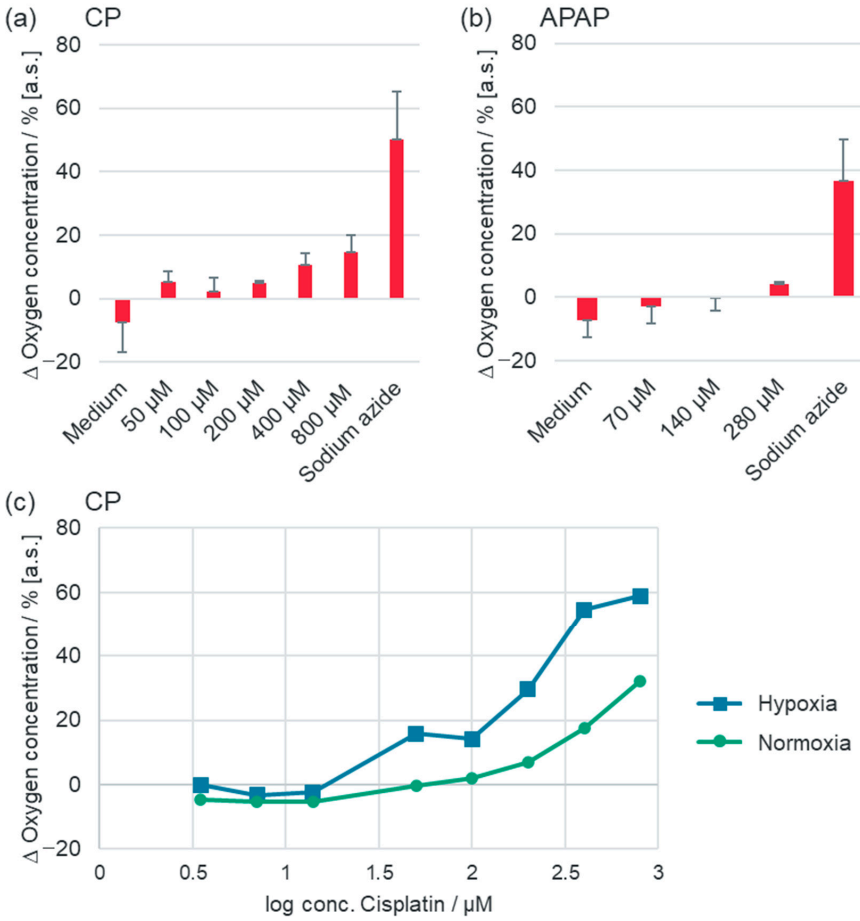

Figure 8. Quantified oxygen changes (%) following additions under normoxic conditions. (**a**) Change in oxygen saturation (%) induced by addition of medium, stepwise increase in cisplatin (CP) concentrations and a final sodium azide administration. Values represent the difference between oxygen saturation immediately prior to each addition and the oxygen level at the last measurable time point before the subsequent addition. Plotted are means ± SD of three independent experiments (n = 3). (**b**) Change in oxygen saturation (%) induced by addition of medium, stepwise increase in acetaminophen (APAP) concentrations, and a final sodium azide administration. Values represent the difference between oxygen saturation immediately prior to each addition and the oxygen level at the last measurable time point before the subsequent addition. Plotted are means ± SD of five independent experiments (n = 5). (**c**) Dose–response curve for cisplatin in HepG2 spheroids under normoxic (green) and hypoxic (blue) conditions. The change in oxygen saturation (%) is plotted against the logarithm of cisplatin concentration (µM). Values represent the cumulative change in oxygen saturation following sequential compound additions (no single-dose tests were performed).

To complement these findings and provide an orthogonal assessment of APAP-induced cytotoxicity, parallel LDH assays and live/dead fluorescence microscopy were performed on HepG2-GFP spheroids under normoxic conditions (Appendix A, Figure A1). These viability data revealed a slight, dose-dependent increase in cell death, confirm-

ing cytotoxic trends while indicating overall high spheroid viability within the tested APAP concentrations.

In the dose–response experiments, spheroids cultured under hypoxic conditions generally showed a reduced sensitivity to acetaminophen compared to normoxic controls. Under hypoxia, higher concentrations of APAP and cisplatin were often required to achieve the same degree of inhibition of mitochondrial respiration (i.e., increase in oxygen saturation) seen under normoxia. Additionally, the onset of mitochondrial inhibition was sometimes delayed in hypoxic spheroids, and in some cases, partial recovery of oxygen consumption was observed after initial inhibition. These findings suggest that hypoxic preconditioning can confer a degree of metabolic resistance to drug-induced mitochondrial dysfunction, likely due to cellular adaptation mechanisms such as increased glycolytic activity and reduced reliance on oxidative phosphorylation. However, for cisplatin (see Figure 8c), we observed the opposite effect: hypoxic spheroids exhibited increased sensitivity, with mitochondrial inhibition occurring at lower concentrations than under normoxic conditions. This indicates that the impact of oxygenation on drug response is compound-dependent and should be carefully considered in experimental design and interpretation.

3.6. Quantifying Cellular Recovery: The Oxygen Consumption Recovery Rate (OCRR)

In order to investigate the recovery capacity of HepG2 spheroids under hypoxic and normoxic conditions after exposure to mitochondrial inhibitors like acetaminophen, we defined a new parameter termed OCRR (oxygen consumption recovery rate). Based on the OCR (oxygen consumption rate), the OCRR determines how rapidly oxygen saturation returned towards baseline levels. By calculating the maximum decrease in oxygen saturation after dose administration it was possible to determine the recovery capacity of the HepG2 spheroids. At acetaminophen dosage (70–280 µM), a decreasing dose-dependent recovery capacity was observed due to the sustained inhibition of mitochondrial respiration in HepG2 spheroids (Figure 9). Furthermore, an increased OCRR under hypoxic conditions was detected. This suggests that mitochondrial respiration was less susceptible to acetaminophen-induced inhibition under hypoxic conditions.

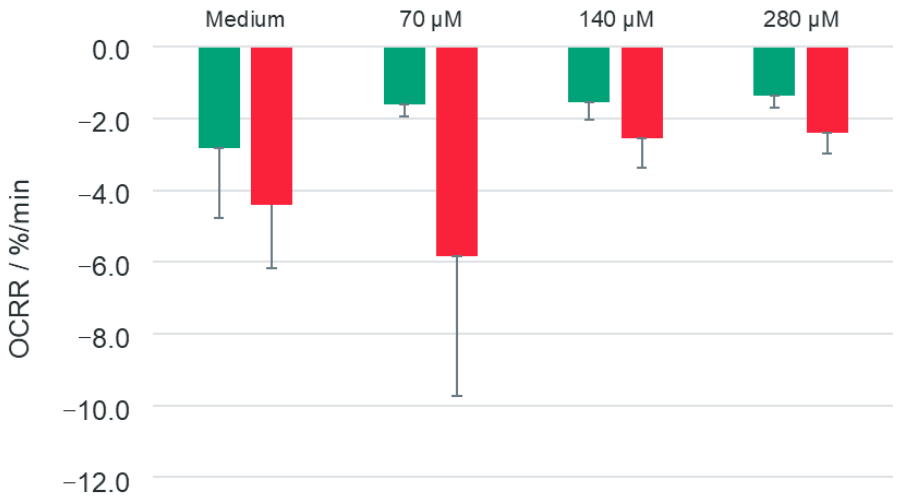

Figure 9. Oxygen Consumption Recovery Rate (OCRR) for APAP dose tests comparing normoxic and hypoxic conditions. The graph displays the OCRR values for HepG2 spheroids treated with Acetaminophen (APAP) under normoxic (green) and hypoxic (red) cultivation conditions. OCRR, defined as the largest negative rate of change between the respiration peak and the subsequent return to a plateau after dose administration, serves as a metric for the cells' recovery capacity following drug exposure. Values are presented as means ± SD from five independent experiments (n = 5).

Statistical analysis using a two-sided Mann–Whitney U-Test revealed no significant differences ($p < 0.05$) between the normoxic and hypoxic conditions at the tested APAP concentrations (70 µM, 140 µM, 280 µM). However, the OCRR analysis showed a tendency towards faster recovery under hypoxic conditions compared to normoxia, indicating a potential modulation of cellular response to APAP depending on oxygen availability.

3.7. Development of Microfluidic Platforms

The development of the microfluidic platform began with preliminary experiments using flexible tubing and three-way stopcocks to manually control fluid flow and simulate medium exchange and reagent addition. To advance towards automation, a system was constructed, incorporating miniature valves (memetis GmbH, Karlsruhe, Germany) and a custom electronic control circuit to test automated valve switching, flow stability, and integration with microcavity arrays. This setup enabled systematic evaluation of valve performance, leakage, and responsiveness under various flow conditions. Based on these insights, a fully integrated chip-based microfluidic platform was ultimately realized, allowing precise, automated control of medium perfusion, gas exchange, and substance addition in dynamic 3D cell culture experiments. The design and functionality of this chip-based platform are detailed in Section 2.14.1.

The microfluidic system enabled flexible and modular 3D cell culture experiments with HeLa cells (Figure 10). In a typical setup, 5×10^4 HeLa cells in 30 µL were seeded onto a microcavity array and pre-incubated for 2 h in a 12-well plate under standard conditions. The array was then transferred into the sterilized and rinsed micro-bioreactor, where it was perfused with complete medium at 400 µL/min. A 10 mL Falcon tube served as the reservoir and bubble trap, and oxygen supply was restricted to diffusion through a TFE membrane in the oxygenator, which was continuously perfused. The system was incubated for 48 h, after which cell viability and morphology were assessed by light microscopy and confocal microscopy. Live/dead staining with SYTO™16 and propidium iodide was performed by introducing the staining solutions via the fluidics and incubating for 2 h before washing and imaging.

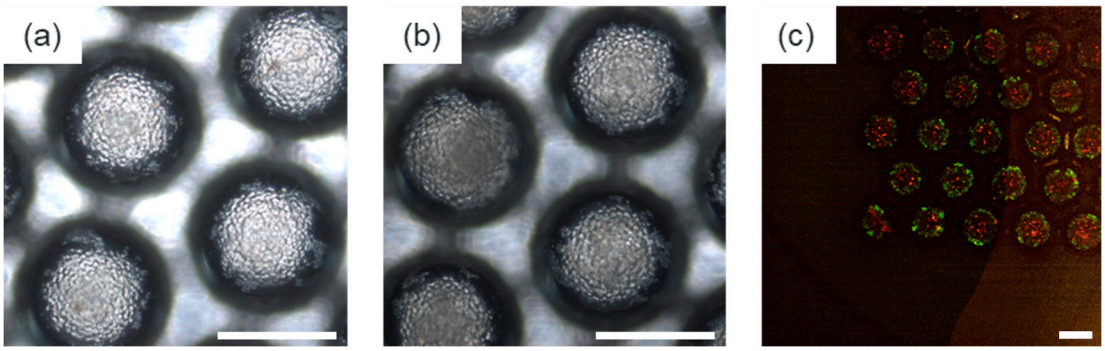

Figure 10. (**a**) HeLa cell culture after 24 h incubation following seeding of 5×10^4 cells in 30 µL onto MicroSpheres and transfer into the microfluidic reactor (continuous perfusion with complete medium at 400 µL/min). (**b**) HeLa cell culture after 48 h incubation (end of experiment). (**c**) Live–dead staining result (SYTO™16/Propidium iodide): maximum projection of the fluorescence signal of both dyes (green = viable cells, stained with SYTO™16, red = dead cells, stained with propidium iodide). (Scale bars: 300 µm).

Results showed well-filled and evenly structured cavities at seeding. After 24 h, cavity edges remained sharply defined, while the centers became blurred—a trend that intensified over 48 h. Live/dead staining revealed cell death (red) in the centers of spheroids, while viable cells (green) persisted in the peripheral regions. This pattern suggests spheroid

formation with central hypoxia and necrosis, consistent with oxygen gradients in 3D cultures. The effect was further pronounced in hypoxia experiments, where the oxygenator was bypassed, resulting in global hypoxia throughout the culture, as confirmed by hypoxia-marker staining and confocal imaging (Figure 11).

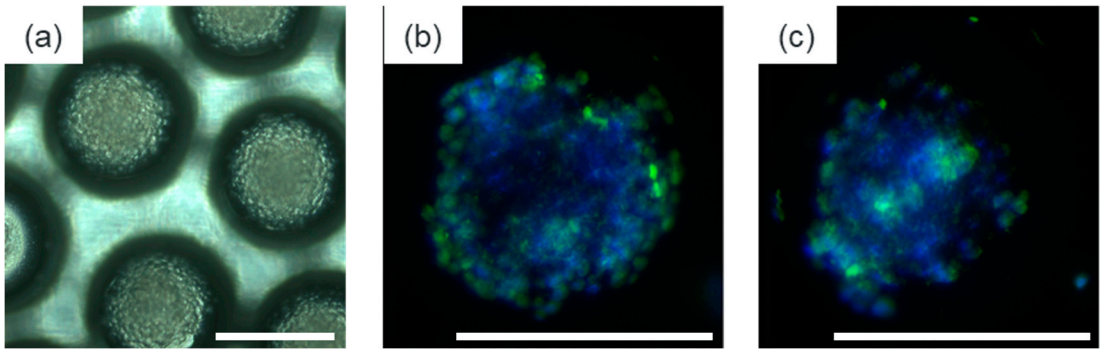

Figure 11. (**a**) MicroSpheres after 96 h cultivation of HeLa spheroids (seeded at 2×10^4 cells per array) (end of experiment). (**b**,**c**) Hypoxia staining results for two representative cavities (pimonidazole/HIF-1α detection with fluorescent secondary antibody in red; nuclei counterstained (blue)). Images show the maximum projection of the fluorescence signal of the hypoxia marker and the nuclear dye. (Scale bars: 300 µm).

The platform proved highly adaptable, allowing rapid configuration with variable tubing, adapters, and connectors—reducing leakage risk and facilitating the integration of diverse components without bonding. PTFE membrane seals provided reliable, leak-free operation, even after repeated assembly. However, in some runs, channel blockages were observed due to over-extruded PETG components, which may have contributed to insufficient oxygen supply and increased central cell death. Overall, these results demonstrate the suitability for dynamic 3D cell culture and oxygen-controlled experiments, while highlighting the importance of precise channel fabrication and membrane integration for robust long-term perfusion.

3.8. The OxyFloat Platform

In this approach, a compact platform ("OxyFloat") was developed to integrate channels, valves, and, if needed, the reactor into a single unit, thereby minimizing system volume and reagent consumption compared to the microfluidic prototype (Figure 12). The platform consisted of a photopolymer 3D-printed Veroclear deck plate with integrated channels on the underside, connected vertically to functional modules via straight risers. The fluid-contacting deck plate could be rapidly iterated and prototyped, while the channel underside was sealed with an ePTFE gasket compressed by a 3D-printed PETG baseplate, providing mechanical stability and resistance to incubator conditions. To address the need for reliable fluidic connections, various connector concepts were evaluated. While commercially available connectors offered flexibility, they introduced excessive dead volume. A custom 3D-printable threaded connector with a continuous 1 mm channel and sealing ring was designed, but its large footprint conflicted with miniaturization goals. Ultimately, the design was refined to employ simple, integrated hose barbs for all fluidic interfaces.

The design objective for the OxyFloat platform was to miniaturize the entire system, to fit the ANSI-standard microtiter plate format (127.76×85.48 mm^2), enabling compatibility with standard microscope stages. A grid of 3×4 M3 screw holes was established, with a 2 mm edge distance to prevent material failure, resulting in nearly symmetrical 40 mm spacing between holes—dimensions informed by previous positive experience with oxygenators using screw spacings of 45–75 mm. The largest component, the pump

with its driver, was positioned first, along with additional chip-mounted hose barbs for tubing connections. Downstream of the pump, the microbioreactor was placed to utilize the observed mixing effect of the pump for even distribution of substances. The valve array was arranged to minimize channel length, bends, and branches, and was divided into two groups: one controlling flow through the oxygenator and the other managing exchange with reservoirs. On the opposite side of the pump, two 40 × 40 mm compartments were reserved for the reservoirs and oxygenator. Reservoir holders were adapted from the prototype setup, while the oxygenator was newly designed with a vertically oriented, significantly reduced gas exchange membrane.

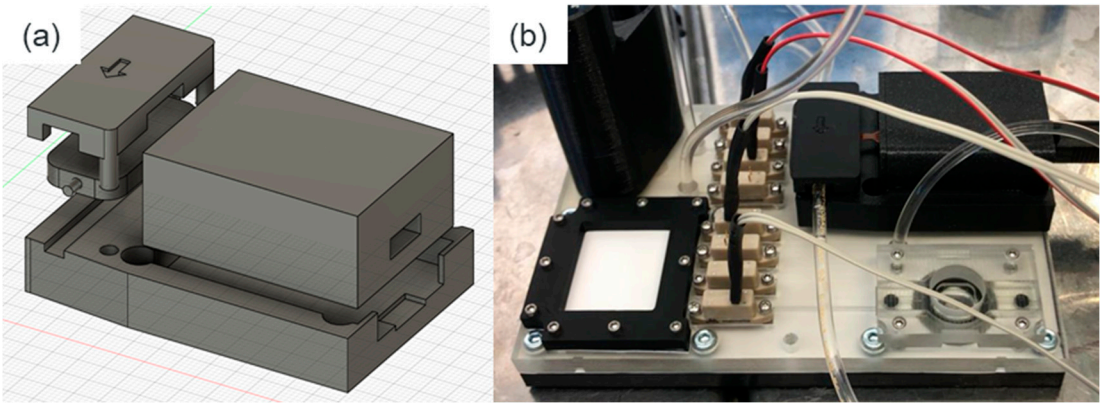

Figure 12. Pump assembly and integration into the OxyFloat platform. (**a**) CAD model of the pump holder with mounted micropump and driver (example: Bartels mp6 micropump and mp6-OEM driver); holder features secure fixation, vibration damping and plug-in tubing/electrical connections. The arrow shows the direction of the medium flow. (**b**) Pump assembly integrated into the OxyFloat deck plate, showing pump inlet/outlet routing, electrical connector and mechanical mounting points within the platform chassis.

The OxyFloat platform integrates several specialized components to enable dynamic 3D cell culture experiments. Fluid transport is achieved using a mp6 micropump (Bartels Mikrotechnik, Dortmund, Germany), controlled by a Bartels mp6-OEM driver module. Flow switching is managed by eight miniature bistable 2/2-way valves (memetis GmbH, Karlsruhe Germany, type 2/2 NC), which are electronically actuated via a custom control circuit. The fluidic deck plate is fabricated from Veroclear photopolymer using a Stratasys Objet260 Connex3 printer, while the sealing baseplate is produced from PETG via FDM 3D printing (BambuLab P1P). Fluidic channels are sealed against the deck plate using an ePTFE gasket (Gore GR sheet, thickness 0.5 mm). The system includes integrated reservoirs compatible with 15 mL Falcon tubes, held by custom 3D-printed adapters. The oxygenator features a vertically oriented ePTFE membrane, and all tubing connections are made via integrated hose barbs (ID 1 mm) for minimal dead volume and secure connections.

The platform passed the leakage tests for all modes of operation successfully but the deck plate deformed under incubation, probably due to the low glass transition temperature of Veroclear resin, which caused leaking. Therefore, further investigation on the plat-form is to be conducted using different materials for the deck plate.

4. Discussion

While the initial application of the SensoSpheres technology was introduced as a proof-of-concept in our previous work [36], this present publication represents a comprehensive advancement and optimization, significantly broadening the platform's applicability and scientific rigor for advanced 3D cell culture research. In contrast to the foundational study, which focused on introducing the basic measurement principle, this work demonstrates a

substantial leap in methodological robustness and practical utility. We have not only refined fundamental aspects, such as optimizing handling protocols and establishing a more robust, multi-device compatible calibration method, but also expanded the technological scope. A key improvement is the successful adaptation of ratiometric oxygen sensing to standard confocal (Leica SP5, Zeiss Axio Observer) and widefield (Leica THUNDER Imager) microscopes. This crucial step decouples the technology from specialized hardware, making it accessible to any well-equipped cell biology lab, thereby significantly enhancing its practical utility and impact. Furthermore, this study delves deeper into application scenarios, presenting rigorous dose–response tests for clinically relevant compounds and providing a foundational outlook on its integration into sophisticated microfluidic organ-on-chip systems. A critical aspect of this study involves the precise terminology used to define oxygen conditions. While traditional cell culture often refers to atmospheric oxygen levels (approx. 18.5% O_2 in incubator medium) as 'normoxia,' a growing body of literature, which we adhere to, defines 'normoxia' as physioxia: the tissue-specific physiological oxygen concentrations experienced by cells in vivo [16,17,21,42]. This distinction is crucial because for many cell types, including the HepG2 cells used here, atmospheric oxygen levels already represent a hyperoxic state relative to their actual physiological environment (liver physioxia: 4–7% O_2 [38,39,43]). Scheidecker et al. demonstrated that primary rat hepatocytes in vitro require approximately 10% O_2 under high diffusive flux to maintain stable, zonation-typical functions, defining this range as their physiological norm [43]. Below 5% O_2, these primary cells rapidly experience energy stress and metabolic reprogramming towards an ischemic/hypoxic response, which is considered non-physiological. Therefore, our classifications of 'hypoxia' (oxygen saturation just above 0%), 'normoxia' (4–7% O_2 saturation), and 'hyperoxia' (above 40% O_2 saturation) are consistently applied throughout this manuscript with reference to human liver tissue physioxia. We acknowledge that our 'hyperoxia' condition, although 'sub-atmospheric' in absolute terms, is biologically hyperoxic for liver cells as it significantly exceeds their physiological needs. This physiologically driven nomenclature provides more relevant insights into cellular responses than a mere comparison to ambient air.

Despite their malignant nature, HepG2 cells, as a hepatocellular carcinoma cell line, still operate within the physiological oxygen constraints of the liver. Given that the maximum physiological oxygen concentration in the liver, even in highly oxygenated areas like the hepatic artery and parenchyma, rarely exceeds 10% O_2, the standard 18.5 to 20% O_2 commonly used in cell culture must be considered hyperoxic even for these cancer cells [43]. This highlights that while HCC cells show remarkable adaptability to low oxygen, their optimal growth and metabolic responses are still framed by physiological boundaries, making hyperoxic culture conditions potentially misleading. Indeed, Baek et al. [44] demonstrated the significant heterogeneity of HCC, where different tumor cell populations exhibit distinct oxygen preferences, thriving from normoxic to strongly hypoxic conditions (below 0.7 mg L^{-1}), with PDX models confirming aggressive behavior in highly hypoxic environments for certain HCC types. While acknowledging the inherent differences in oxygen delivery mechanisms between a perfused in vivo tissue and our diffusion-limited in vitro system, our approach prioritizes replicating the pericellular oxygen microenvironment that cells truly experience.

For initial variants, the formed microcavity arrays were placed in CellCrowns™. Compared to those where the arrays were directly welded to an insert, disadvantages were particularly evident in handling. Since the connection is not always tight when placed in the inserts, medium must be filled into the surrounding well. This is not only an additional step, but it also complicates the introduction of cells. The welded films showed more uniform spheroids and the reproducibility of the calibration was also increased.

In the past, formed films were mostly disinfected only with isopropanol. After several contaminations, the protocol was extended to include sodium azide. This reliably prevented contaminations. It was also tested whether autoclaving is a viable option. For the inserts themselves, this worked, but the fluorescence intensity of the sensor films was so strongly reduced by autoclaving that this method was not pursued further.

Oxygen measurement with the MicrosCube systems from PreSens provides a reliable and rapid method for long-term monitoring. A key advancement presented here is the successful adaptation of this ratiometric oxygen sensing method to standard confocal (Leica SP5, Zeiss Axio Observer) and widefield (Leica THUNDER Imager) microscopes. This is significant because it decouples the technology from specialized hardware, making it accessible to any well-equipped cell biology lab. The transition to high-content microscopic imaging generated large, complex datasets, that necessitated the development of novel analytical workflows. For this, we established a semi-automated analysis pipeline, combining tools like CellProfiler™ and custom-written Python scripts.

The THUNDER Imager, with its rapid acquisition speed and computational clearing, proved particularly advantageous for high-throughput applications. More importantly, this integration opens the door for simultaneous multi-parameter imaging, such as correlating pericellular oxygen concentration with intracellular calcium signaling in real-time, as we have previously demonstrated with iPSC-derived cardiomyocytes [35]. These contain a genetically encoded calcium sensor that shows a fluorescence signal upon calcium influx. Thus, for example, the beating frequency can be determined. In a previous approach (Grün 2023), this had to be measured sequentially.

Preliminary results using a Zeiss Axio Observer further confirm the platform's compatibility with a broad range of standard microscopy systems. Looking forward, the integration with ultra-fast volumetric imaging technologies, such as the ZEISS LSM Lightfield 4D, holds particular promise. Its ability to capture entire volumes at high speed could enable rapid, parallel ratiometric measurements across hundreds of spheroids, dramatically increasing the throughput for oxygen-dependent studies.

Furthermore, with confocal techniques, it is possible to generate true 3D information with a significantly higher resolution.

The image analyses in this study were conducted using CellProfiler™ and for live tracking the Live- MITOS plugin. Overall, both tools proved to be reliable and suitable for evaluating fluorescence-based oxygen measurements. However, several practical limitations became apparent during use. ROI detection was occasionally affected by condensate formation, which was a physical artifact through handling rather than a software-related issue. In addition, variations in image brightness sometimes hindered consistent ROI identification. During live measurements, the addition of substances occasionally caused plate displacement, resulting in a misalignment of the ROI identifying mask, which for live tracking was only applied to the first frame. Consequently, continuous live tracking across the time series was not possible, although a later plugin version reportedly resolved this issue. Moreover, CellProfiler™ assigns microcavity numbers randomly, complicating the tracking of individual cavities across different measurements and making this possible only through the Live- MITOS plugin. A further limitation of the analysis lies in its restriction to two-dimensional image data, which prevents the assessment of spatial variations in oxygen distribution along the *z*-axis.

Our results demonstrate that physiologically relevant oxygen levels, from hyperoxia down to severe hypoxia (~1.8% O_2), can be reliably established and maintained in standard multi-well plates simply by adjusting the medium height. This provides a low-cost, high-throughput alternative to expensive and complex hypoxia chambers. The validation of these conditions using molecular markers like HIF-1α confirms that our platform induces a

true physiological hypoxic response. In the literature, hypoxia is defined as the range below 3% oxygen [45–49]. In our proof-of-concept experiment, we were able to reach a value of 1.8% oxygen with a maximum filling level in the well (Figure 6). The HIF-1α staining also showed the expression of HIF-1α, an indication of hypoxia (Figure 7). This was confirmed by pimonidazole staining (Figure 7). Hyperoxia is defined as around 20% oxygen [45–49]. By reducing the medium volume, we were able to achieve 19.6% (Figure 6). We define normoxia as an oxygen concentration between hypoxia and hyperoxia. In our case, this was defined as the state in which we cultivate the cells under our standard conditions. In the literature, normoxia is not precisely defined. However, it is important here to distinguish between normoxia and physioxia. In our setup, the oxygen saturation was 4.1% (Figure 6). For primary liver cells, a physioxic oxygen concentration in the range of 4–7.2% [17,38] or more precisely at 5.4% [38,39] is reported. The applicability of our platform extends beyond liver models to the recreation of complex, physiologically relevant microenvironments, such as the hematopoietic stem cell (HSC) niche. The bone marrow niche is inherently hypoxic, making precise oxygen control critical for modeling its function. In related experiments, we have successfully established co-cultures of leukemic cells (e.g., HL-60) and stromal cells (HS-5) in our MicroSpheres under hypoxic and glucose-deprived conditions. This demonstrates the platform's capability to model complex microenvironments and its potential for studying how niche-specific parameters might modulate the expression of key leukemia-associated markers, including Gpr56 and CLL-1, to gain insights into clonal selection and therapeutic resistance in hematological malignancies.

In subsequent experiments, the dose–response assays for cisplatin and acetaminophen were expanded and refined. Testing lower cisplatin concentrations (3.5, 7, and 14 µM) confirmed the high sensitivity of HepG2 spheroids, which showed a clear inhibition of mitochondrial respiration even in this range. At higher concentrations (up to 800 µM), both HepG2 and HeLa spheroids exhibited a rapid and sustained increase in oxygen saturation, indicating strong mitochondrial inhibition and eventual cell death.

For APAP, it was noticed that DMSO as a solvent biased the results; switching to $PBS^{+/+}$ for stock solution preparation significantly improved assay reliability. Subsequently, APAP concentrations of 70, 140, and 280 µM were tested, which showed a dose-dependent mitochondrial inhibition. These experiments contributed significantly to a better definition of the dose ranges, the optimization of protocol robustness (solvent selection), and the confirmation of dose-dependent effects over a broader concentration spectrum.

With the definition of the Oxygen Consumption Recovery Rate (OCRR), we introduce a new, quantitative parameter to evaluate cellular recovery capacity after drug-induced mitochondrial inhibition. Unlike simple endpoint measurements, the OCRR captures the dynamic recovery of cellular respiration in real time and provides insight into the resilience of the spheroids. In our experiments with APAP, a tendency to a dose-dependent decrease in OCRR was observed, indicating that the recovery capacity of the cells decreases with increasing drug concentration. Interestingly, we observed an increased OCRR under hypoxic conditions, which supports the assumption that hypoxia-adapted cells are less susceptible to APAP-induced mitochondrial damage.

The OCRR thus offers a significant added value compared to traditional toxicity assays: it allows not only the quantification of inhibition but also of cellular compensation and repair mechanisms. This parameter could be of great importance in the future for detecting subtle differences in cytotoxicity and significantly increasing the predictive power of in vitro models for drug development.

The successful application of assays like the 3D Mito-Stress Test for substance evaluation is highly dependent on the quality and viability of the spheroids. Our findings are consistent with previous work of our group, which demonstrated that reproducibility can

be compromised by suboptimal culture conditions, leading to a high percentage of dead cells and, consequently, a lack of cellular response to mitochondrial inhibitors (unpublished data). This underscores the importance of the optimized handling and cultivation protocols presented in this study, such as the use of BIOFLOAT™ coating and adjusted seeding densities, which are critical for generating robust and reliable data in dose–response assays. By ensuring high spheroid viability, we could attribute the observed changes in oxygen consumption specifically to the effects of cisplatin and acetaminophen, rather than to baseline culture instability.

The integration of our SensoSpheres into microfluidic platforms is a crucial step towards creating dynamic, physiologically relevant in vitro models, such as organ-on-chips. As demonstrated with a microfluidic system, our system allows for the continuous perfusion of 3D cell cultures, which is essential for long-term viability and for mimicking systemic effects like drug delivery and clearance. The results from perfusing HeLa spheroids confirm that the platform, even in its prototype stage, can maintain viable cultures for up to 48 h. The observation of central necrosis in these spheroids, which was more pronounced when the oxygenator was bypassed, strongly suggests that oxygen gradients are a decisive factor for cell fate in these dynamic 3D models. This validates that our system can be used to study hypoxia-related phenomena in a controlled perfusion environment.

The development of the compact OxyFloat platform in a microtiter plate format was a direct response to the limitations of our prototypes using longer tubings, aiming to reduce dead volume and improve system integration. While initial tests with the OxyFloat platform showed successful fluidic operation, material challenges, such as the deformation of the Veroclear deck plate under incubation conditions, highlight the need for further material optimization; for example, by using polycarbonate. Nevertheless, these proof-of-concept experiments demonstrate the clear potential of combining our sensor array technology with microfluidics to create advanced organ-on-a-chip systems for high-content analysis and predictive substance testing.

5. Conclusions

In this work, we have established a robust and versatile platform for the real-time, spatially resolved analysis of oxygen dynamics in 3D cell cultures. By optimizing key methodological aspects, from fabrication and handling to calibration and data analysis, we have transformed a promising technology into a reproducible tool for advanced biological research. The transition from leak-prone CellCrown™ inserts to custom-welded inserts was a critical step in ensuring system tightness and thus, the reproducibility of long-term assays. Similarly, the establishment of a robust sodium azide/isopropanol sterilization protocol was fundamental to overcoming contamination issues without compromising the sensor's fluorescence properties, a significant limitation of methods like autoclaving.

While this foundational study primarily utilized spheroids for validation, the platform's versatility has already been demonstrated in more complex models. Its successful application with iPSC-derived cardiomyocytes [35] highlights its suitability for functional metabolic assays, while preliminary results from co-culture models of the hematopoietic stem cell (HSC) niche (unpublished data) underscore its potential for studying complex cell–cell interactions. The flexibility of the microthermoforming process further ensures the system is readily adaptable for the culture of larger, more complex organoids.

Looking forward, the successful proof-of-concept from our initial microfluidic experiments underscores the platform's significant potential for integration into advanced organ-on-chip (OoC) systems. Enabling the study of 3D cell models under dynamic perfusion is the next critical step toward mimicking systemic effects like drug clearance and chronic exposure. By facilitating the creation of more predictive and physiologically

relevant in vitro models, this work provides a powerful tool to refine preclinical drug development and ultimately contribute to the goal of reducing animal testing.

Author Contributions: Conceptualization, E.G. and C.G.; Methodology, C.G., E.S., J.t.H. and M.K.; Formal Analysis, M.K., E.S., J.t.H., C.D., C.B. and E.G.; Investigation, M.K., E.S., J.t.H., C.D., C.B. and L.F.; Resources, C.N.; Writing—Original Draft Preparation, C.G.; Writing—Review and Editing, all authors; Visualization, C.G.; Supervision, E.G., C.N. and C.G.; Project Administration, E.G. and C.G.; Funding Acquisition, C.G. and E.G. All authors have read and agreed to the published version of the manuscript.

Funding: This research was funded by the Helmholtz Initiative and Networking Fund, grant number HE-2023-11.

Institutional Review Board Statement: Not applicable.

Informed Consent Statement: Not applicable.

Data Availability Statement: The original contributions presented in this study are included in the article. Further inquiries can be directed to the corresponding author.

Acknowledgments: The authors thank Domenik Fischer and Muhammad Qasim (both Karlsruhe Institute of Technology, KIT, Germany) for their crucial support in mechanical design and for developing the Python script for automated image analysis, respectively. We also thank Michelle Rottmann, Sabrina Denzer, Sophie Czerny, and Sarah Ahmad (KIT, Germany) for their general support in the lab. We further thank Jonas Wohlgemuth (KIT, Germany) for 3D printing of some of the OxyFloat platform components. We extend our sincere gratitude to Gregor Liebsch from PreSens Precision Sensing GmbH for his invaluable support with their measurement devices and for his expert assistance in instrument operation and data analysis. Furthermore, we would like to acknowledge Steffen Burgold, Martin Jeworski, and Noemi Castroviejo Jimenez from Zeiss for providing the opportunity to use their advanced microscopy systems and for their helpful support during data acquisition. During the preparation of this manuscript, we used Google's Gemini 2.5 pro for the purpose of improving wording and correcting the English language. We did not use AI to generate, evaluate, or analyze results. We have reviewed and edited the output and take full responsibility for the content of this publication.

Conflicts of Interest: C.G., C.N., and E.G. declare a conflict of interest as co-founders of CAVIGEN, a spin-off from the Karlsruhe Institute of Technology (KIT) that commercializes the microcavity array technology (SensoSphere and MicroSphere) presented in this work. The foundational research described herein was predominantly conducted at KIT prior to the company's establishment, and all three authors continue their primary research activities at the institute. The remaining authors declare no conflicts of interest.

Abbreviations

The following abbreviations are used in this manuscript:

CTG	CellTracker^{TM} green
a.s.	Air saturation
APAP	Acetaminophen
cLSM	Confocal Laser Scanning Microscopy
CP	Cisplatin
HCC	Hepatocellular Carcinoma
hPL	Human Platelet Lysate
KIT	Karlsruhe Institute of Technology
NEAA	Non-Essential Amino Acids
OCRR	Oxygen Consumption Recovery Rate
OoC	Organ-On-Chip
PC	Polycarbonate

PDX Patient-Derived Xenograft
PMMA Poly(methyl methacrylate)

Appendix A

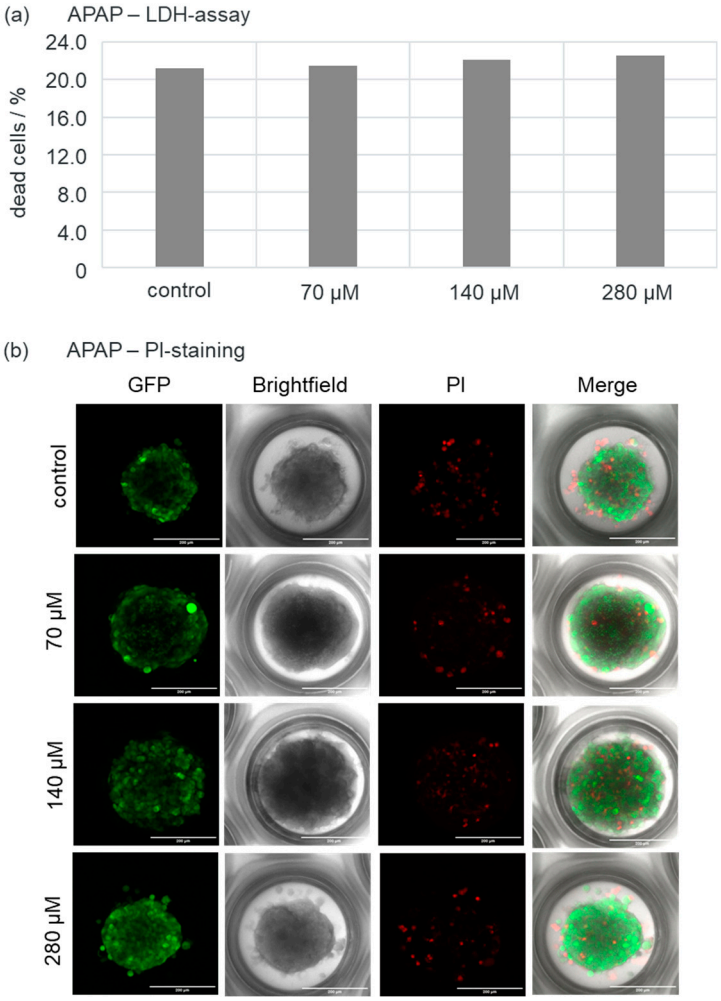

Figure A1. Viability assessment of HepG2-GFP spheroids after Acetaminophen (APAP) treatment under normoxic conditions. This figure provides a comprehensive overview of the cytotoxic effects of APAP on HepG2-GFP spheroids. Spheroids were cultured for two days under normoxic conditions (37 °C, 5% CO_2, 1200 µL medium volume) and then treated with single doses of APAP for one hour at indicated concentrations (70 µM, 140 µM, 280 µM) or a medium control. (**a**) Quantitative cytotoxicity assessment using LDH assay (LDH-Glo^{TM} Cytotoxicity Assay, Promega). The bar chart illustrates the percentage of dead cells [%] determined by the LDH Cytotoxicity Assay. The negative control (medium only) showed 21.20% dead cells, indicating a baseline level of cellular stress or spontaneous cell death in the model. With increasing APAP concentrations, a slight, dose-dependent increase in dead cells was observed: 21.46% at 70 µM, 22.10% at 140 µM, and 22.54% at 280 µM. While the differences are numerically small, they indicate a clear trend towards increased cytotoxicity with higher APAP doses. (**b**) Representative fluorescence microscopy images of HepG2-GFP spheroids. Magnified views of selected HepG2-GFP spheroids are shown for the control and each APAP concentration (70 µM, 140 µM, 280 µM). Each set of images comprises four channels: GFP fluorescence (green) indicating viable cells, brightfield microscopy, propidium iodide (PI) fluorescence (red) indicating dead cells, and a merged overlay of these channels. Visually, compared to the control, all APAP concentrations show high cell viability with only a few PI-positive (red) dead cells. Even at the highest concentration (280 µM), no significant increase in dead cells is apparent. This suggests a low cytotoxic effect of acetaminophen on HepG2-GFP spheroids within the tested concentration range under normoxic conditions. (Scale bar: 200 µm).

References

1. Sun, D.; Gao, W.; Hu, H.; Zhou, S. Why 90% of clinical drug development fails and how to improve it? *Acta Pharm. Sin. B* **2022**, *12*, 3049–3062. [CrossRef]
2. Onakpoya, I.J.; Heneghan, C.J.; Aronson, J.K. Post-marketing withdrawal of 462 medicinal products because of adverse drug reactions: A systematic review of the world literature. *BMC Med.* **2016**, *14*, 10. [CrossRef]
3. Dowden, H.; Munro, J. Trends in clinical success rates and therapeutic focus. *Nat. Rev. Drug Discov.* **2019**, *18*, 495–496. [CrossRef] [PubMed]
4. Harrison, R.K. Phase II and phase III failures: 2013–2015. *Nat. Rev. Drug Discov.* **2016**, *15*, 817–818. [CrossRef] [PubMed]
5. Van Norman, G.A. Limitations of Animal Studies for Predicting Toxicity in Clinical Trials: Is it Time to Rethink Our Current Approach? *JACC Basic Transl. Sci.* **2019**, *4*, 845–854. [CrossRef]
6. Hu, J.; Hu, T.; Guo, Z.; Song, Y.; Shan, L.; Shi, X. Species Difference in the Metabolism of Mulberrin in Vitro and Its Inhibitory Effect on Cytochrome P450 and UDP-Glucuronosyltransferase Enzymes. *Chem. Pharm. Bull.* **2022**, *70*, 669–678. [CrossRef] [PubMed]
7. Cao, Y.; Polacheck, W. New Approach Methodologies: What Clinical Pharmacologists Should Prepare For. *Clin. Pharmacol. Ther.* **2025**, *118*, 1269–1272. [CrossRef]
8. Pierson, J.B.; Bahinski, A.; Berridge, B.; Bramham, D.; Bourcier, T.; Chaudhary, K.W.; Eldridge, S.; Kanda, Y.; Mattes, W.B.; Oliphant, J.; et al. Validating and Using Cardiac NAMs for Toxicity Screening and Drug Development. *Int. J. Toxicol.* **2025**, *44*, 499–506. [CrossRef]
9. Mehta, K.; Maass, C.; Cucurull-Sanchez, L.; Pichardo-Almarza, C.; Subramanian, K.; Androulakis, I.P.; Gobburu, J.; Schaller, S.; Sherwin, C.M. Modernizing Preclinical Drug Development: The Role of New Approach Methodologies. *ACS Pharmacol. Transl. Sci.* **2025**, *8*, 1513–1525. [CrossRef]
10. Moscona, A. The development in vitro of chimeric aggregates of dissociated embryonic chick and mouse cells. *Proc. Natl. Acad. Sci. USA* **1957**, *43*, 184–194. [CrossRef]
11. Holtfreter, J. A study of the mechanics of gastrulation. *J. Exp. Zool.* **1944**, *95*, 171–212. [CrossRef]
12. Li, D.-W.; He, F.-L.; He, J.; Deng, X.; Liu, Y.-L.; Liu, Y.-Y.; Ye, Y.-J.; Yin, D.-C. From 2D to 3D: The morphology, proliferation and differentiation of MC3T3-E1 on silk fibroin/chitosan matrices. *Carbohydr. Polym.* **2017**, *178*, 69–77. [CrossRef]
13. Yamada, K.M.; Doyle, A.D.; Lu, J. Cell–3D matrix interactions: Recent advances and opportunities. *Trends Cell Biol.* **2022**, *32*, 883–895. [CrossRef]
14. Rybkowska, P.; Radoszkiewicz, K.; Kawalec, M.; Dymkowska, D.; Zabłocka, B.; Zabłocki, K.; Sarnowska, A. The Metabolic Changes between Monolayer (2D) and Three-Dimensional (3D) Culture Conditions in Human Mesenchymal Stem/Stromal Cells Derived from Adipose Tissue. *Cells* **2023**, *12*, 178. [CrossRef] [PubMed]
15. Altmann, B.; Giselbrecht, S.; Weibezahn, K.-F.; Welle, A.; Gottwald, E. The three-dimensional cultivation of the carcinoma cell line HepG2 in a perfused chip system leads to a more differentiated phenotype of the cells compared to monolayer culture. *Biomed. Mater.* **2008**, *3*, 034120. [CrossRef]
16. Barakat, S.; Yang, F.; Yelkenci, H.E.; Kök, K.; Mann, G.E.; Eroğlu, E. Proteomic Data and Drug Implications for Cerebral Microvascular Endothelial Cells Under Varying Oxygen Levels. *Sci. Data* **2025**, *12*, 989. [CrossRef] [PubMed]
17. Keeley, T.P.; Mann, G.E. Defining Physiological Normoxia for Improved Translation of Cell Physiology to Animal Models and Humans. *Physiol. Rev.* **2019**, *99*, 161–234. [CrossRef]
18. Vicente, P.; Almeida, J.I.; Crespo, I.E.; Virgolini, N.; Isidro, I.A.; Calleja-Cervantes, M.E.; Rodriguez-Madoz, J.R.; Prosper, F.; Alves, P.M.; Serra, M. Oxygen control in bioreactor drives high yield production of functional hiPSC-like hepatocytes for advanced liver disease modelling. *Sci. Rep.* **2024**, *14*, 24599. [CrossRef]
19. Alva, R.; Gardner, G.L.; Liang, P.; Stuart, J.A. Supraphysiological Oxygen Levels in Mammalian Cell Culture: Current State and Future Perspectives. *Cells* **2022**, *11*, 3123. [CrossRef]
20. Walaas, G.A.; Gopalakrishnan, S.; Bakke, I.; Skovdahl, H.K.; Flatberg, A.; Østvik, A.E.; Sandvik, A.K.; Bruland, T. Physiological hypoxia improves growth and functional differentiation of human intestinal epithelial organoids. *Front. Immunol.* **2023**, *14*, 1095812. [CrossRef]
21. Alva, R.; Wiebe, J.E.; Stuart, J.A. Revisiting reactive oxygen species production in hypoxia. *Pflug. Arch.* **2024**, *476*, 1423–1444. [CrossRef]
22. Allen, J.W. In Vitro Zonation and Toxicity in a Hepatocyte Bioreactor. *Toxicol. Sci.* **2005**, *84*, 110–119. [CrossRef]
23. Peng, C.-C.; Liao, W.-H.; Chen, Y.-H.; Wu, C.-Y.; Tung, Y.-C. A microfluidic cell culture array with various oxygen tensions. *Lab Chip* **2013**, *13*, 3239. [CrossRef] [PubMed]

24. Dornhof, J.; Zieger, V.; Kieninger, J.; Frejek, D.; Zengerle, R.; Urban, G.A.; Kartmann, S.; Weltin, A. Bioprinting-based automated deposition of single cancer cell spheroids into oxygen sensor microelectrode wells. *Lab Chip* **2022**, *22*, 4369–4381. [CrossRef]
25. Clark, L.C., Jr.; Wolf, R.; Granger, D.; Taylor, Z. Continuous Recording of Blood Oxygen Tensions by Polarography. *J. Appl. Physiol.* **1953**, *6*, 189–193. [CrossRef]
26. Whalen, W.J.; Nair, P.; Ganfield, R.A. Measurements of oxygen tension in tissues with a micro oxygen electrode. *Microvasc. Res.* **1973**, *5*, 254–262. [CrossRef] [PubMed]
27. Rumsey, W.L.; Vanderkooi, J.M.; Wilson, D.F. Imaging of phosphorescence: A novel method for measuring oxygen distribution in perfused tissue. *Science* **1988**, *241*, 1649–1651. [CrossRef] [PubMed]
28. Dmitriev, R.I.; Papkovsky, D.B. Optical probes and techniques for O2 measurement in live cells and tissue. *Cell. Mol. Life Sci.* **2012**, *69*, 2025–2039. [CrossRef]
29. Wang, X.D.; Wolfbeis, O.S. Optical methods for sensing and imaging oxygen: Materials, spectroscopies and applications. *Chem. Soc. Rev.* **2014**, *43*, 3666–3761. [CrossRef]
30. Soares, A.B.; Meier, R.; Liebsch, G.; Schwenk-Zieger, S.; Kirmaier, M.E.; Theurich, S.; Widmann, M.; Canis, M.; Gires, O.; Haubner, F. High-resolution spatiotemporal pH_e and pO_2 imaging in head and neck and oesophageal carcinoma cells. *Cancer Metab.* **2021**, *9*, 21. [CrossRef]
31. Liebsch, G.; Klimant, I.; Frank, B.; Holst, G.; Wolfbeis, O.S. Luminescence Lifetime Imaging of Oxygen, pH, and Carbon Dioxide Distribution Using Optical Sensors. *Appl. Spectrosc.* **2000**, *54*, 548–559. [CrossRef]
32. Tschiersch, H.; Liebsch, G.; Stangelmayer, A.; Borisjuk, L.; Rolletschek, H. Planar Oxygen Sensors for Non Invasive Imaging in Experimental Biology. In *Microsensors*; InTech: London, UK, 2011.
33. Giselbrecht, S.; Gietzelt, T.; Gottwald, E.; Guber, A.; Trautmann, C.; Truckenmüller, R.; Weibezahn, K.-F. Microthermoforming as a novel technique for manufacturing scaffolds in tissue engineering. *IEE Proc. Nanobiotechnol.* **2004**, *151*, 151–157. [CrossRef]
34. Gottwald, E.; Giselbrecht, S.; Augspurger, C.; Lahni, B.; Dambrowsky, N.; Truckenmüller, R.; Piotter, V.; Gietzelt, T.; Wendt, O.; Pfleging, W.; et al. A chip-based platform for the in vitro generation of tissues in three-dimensional organization. *Lab Chip* **2007**, *7*, 777–785. [CrossRef]
35. Grün, C. *Entwicklung eines Verfahrens zur Herstellung von Sauerstoff-Sensitiven 3D-Zellkultursystemen auf Mikrokavitätenarray-Basis*; Karlsruher Institut für Technologie (KIT): Karlsruhe, Germany, 2023.
36. Grün, C.; Pfeifer, J.; Liebsch, G.; Gottwald, E. O_2-sensitive microcavity arrays: A new platform for oxygen measurements in 3D cell cultures. *Front. Bioeng. Biotechnol.* **2023**, *11*, 1111316. [CrossRef] [PubMed]
37. Gottwald, E.; Grün, C.; Nies, C.; Liebsch, G. Physiological oxygen measurements in vitro-Schrodinger's cat in 3D cell biology. *Front. Bioeng. Biotechnol.* **2023**, *11*, 1218957. [CrossRef] [PubMed]
38. Leary, T.S.; Klinck, J.R.; Hayman, G.; Friend, P.; Jamieson, N.V.; Gupta, A.K. Measurement of liver tissue oxygenation after orthotopic liver transplantation using a multiparameter sensor. *Anaesthesia* **2002**, *57*, 1128–1133. [CrossRef]
39. Brooks, A.J.; Eastwood, J.; Beckingham, I.J.; Girling, K.J. Liver tissue partial pressure of oxygen and carbon dioxide during partial hepatectomy. *Br. J. Anaesth.* **2004**, *92*, 735–737. [CrossRef] [PubMed]
40. Shirmanova, M.V.; Druzhkova, I.N.; Lukina, M.M.; Dudenkova, V.V.; Ignatova, N.I.; Snopova, L.B.; Shcheslavskiy, V.I.; Belousov, V.V.; Zagaynova, E.V. Chemotherapy with cisplatin: Insights into intracellular pH and metabolic landscape of cancer cells in vitro and in vivo. *Sci. Rep.* **2017**, *7*, 8911. [CrossRef]
41. Baek, N.; Seo, O.W.; Lee, J.; Hulme, J.; An, S.S.A. Real-time monitoring of cisplatin cytotoxicity on three-dimensional spheroid tumor cells. *Drug Des. Dev. Ther.* **2016**, *10*, 2155–2165. [CrossRef]
42. Alva, R.; Mirza, M.; Baiton, A.; Lazuran, L.; Samokysh, L.; Bobinski, A.; Cowan, C.; Jaimon, A.; Obioru, D.; Al Makhoul, T.; et al. Oxygen toxicity: Cellular mechanisms in normobaric hyperoxia. *Cell Biol. Toxicol.* **2023**, *39*, 111–143. [CrossRef]
43. Scheidecker, B.; Shinohara, M.; Sugimoto, M.; Danoy, M.; Nishikawa, M.; Sakai, Y. Induction of in vitro Metabolic Zonation in Primary Hepatocytes Requires Both Near-Physiological Oxygen Concentration and Flux. *Front. Bioeng. Biotechnol.* **2020**, *8*, 524. [CrossRef]
44. Baek, S.; Ha, H.-S.; Park, J.S.; Cho, M.J.; Kim, H.-S.; Yu, S.E.; Chung, S.; Kim, C.; Kim, J.; Lee, J.Y.; et al. Chip collection of hepatocellular carcinoma based on O_2 heterogeneity from patient tissue. *Nat. Commun.* **2024**, *15*, 5117. [CrossRef]
45. Lin, R.-Z.; Chou, L.-F.; Chien, C.-C.M.; Chang, H.-Y. Dynamic analysis of hepatoma spheroid formation: Roles of E-cadherin and β1-integrin. *Cell Tissue Res.* **2006**, *324*, 411–422. [CrossRef] [PubMed]
46. Mazure, N.M.; Pouyssegur, J. Hypoxia-induced autophagy: Cell death or cell survival? *Curr. Opin. Cell Biol.* **2010**, *22*, 177–180. [CrossRef] [PubMed]
47. Carreau, A.; El Hafny-Rahbi, B.; Matejuk, A.; Grillon, C.; Kieda, C. Why is the partial oxygen pressure of human tissues a crucial parameter? Small molecules and hypoxia. *J. Cell. Mol. Med.* **2011**, *15*, 1239–1253. [CrossRef] [PubMed]

48. Stuart, J.A.; Fonseca, J.; Moradi, F.; Cunningham, C.; Seliman, B.; Worsfold, C.R.; Dolan, S.; Abando, J.; Maddalena, L.A. How Supraphysiological Oxygen Levels in Standard Cell Culture Affect Oxygen-Consuming Reactions. *Oxidative Med. Cell. Longev.* **2018**, *2018*, 8238459. [CrossRef]
49. Wenger, R.H.; Kurtcuoglu, V.; Scholz, C.C.; Marti, H.H.; Hoogewijs, D. Frequently asked questions in hypoxia research. *Hypoxia* **2015**, *3*, 35–43. [CrossRef]